J. Fluid Mech. (2001), *vol.* 426, *pp.* 229–262. Printed in the United Kingdom

© 2001 Cambridge University Press

Effect on a laminar boundary layer of small-amplitude streamwise vorticity in the upstream flow

By DAVID W. WUNDROW[1]† AND M. E. GOLDSTEIN[2]

[1] Nyma Inc., Glenn Research Center Group, Cleveland, OH 44135, USA

[2] NASA, Glenn Research Center, Cleveland, OH 44135, USA

(Received 7 July 1998 and in revised form 31 July 2000)

This paper is a generalization of a previous analysis of the effects of a small-amplitude, steady, streamwise vorticity field on the flow over an infinitely thin flat plate in an otherwise uniform stream. That analysis, which is given in Goldstein & Leib (1993), required that the disturbance Reynolds number (i.e. the Reynolds number based on the disturbance velocity and length scale) be infinite while the present paper considers the more general case where this quantity can be finite. The results show how an initially linear perturbation of the upstream flow ultimately leads to a small-amplitude but nonlinear cross-flow far downstream from the leading edge. This flow can, under certain conditions, cause the streamwise velocity profiles to develop distinct shear layers in certain localized spanwise regions. These shear layers, which are remarkably similar to the ones that develop in Tollmien–Schlichting-wave transition (Kovasznay, Komoda & Vasudeva 1962), are highly inflectional and can therefore support the rapidly growing inviscid instabilities that are believed to break down into turbulent spots (Greenspan & Benney 1963, and, subsequently, many others). Numerical computations are carried out for input parameters which approximate the flow conditions of some recent experimental studies of the so-called Klebanoff-mode phenomenon. The results are used to explain some of the experimental observations, and, more importantly, to explain why the averaged quantities usually reported in these experiments do not correlate well with the turbulent-spot formation and therefore with the overall transition process.

1. Introduction

This paper describes a predominantly numerical study of the effects of vortical free-stream disturbances on transition to turbulence in flat-plate boundary layers. Weak free-stream turbulence in an otherwise uniform stream is probably the most important example of this type of disturbance, and Dryden (1936) and Taylor (1939) were the first to study its effects on the flat-plate boundary layer. They showed that the resulting streamwise velocity fluctuations were of very low frequency and reached amplitudes that were several times larger than those in the free stream. Taylor (1939) noted that the velocity fluctuations appear to correspond to a thickening and thinning of the boundary layer, which he accurately modelled using simple heuristic

† Present affiliation: Ohio Aerospace Institute, 22800 Cedar Point Road, Cleveland, OH 44142, USA.

arguments. These low-frequency structures, which are now referred to as Klebanoff modes (Kendall 1991), are not only important in their own right but also because of their possible relation to the wall-layer streaks in a fully turbulent boundary layer.

There have been several theoretical and numerical studies of the effect of small free-stream disturbances on flat-plate boundary layers, but only a few of these actually relate to the Klebanoff modes. Crow (1966) put the original Taylor result on a rational asymptotic basis, by carrying out a linear analysis of the boundary-layer flow due to a steady spanwise distortion of an otherwise uniform free stream. The linearization is valid when either the disturbance Reynolds number $r \equiv \epsilon R_\lambda$ or the appropriately scaled distance from the leading edge (or both) is (are) small. Here R_λ is just the ordinary Reynolds number based on the characteristic length scale λ of the disturbance, and ϵ is its characteristic amplitude. Crow (1966) found that the free-stream distortion produces a streamwise velocity fluctuation that grows linearly with downstream distance and has a shape that agrees exactly with the one proposed by Taylor (1939). Luchini (1996) considered the eigenmode solutions to the linearized boundary-layer equations and found an algebraically growing three-dimensional mode. However, the growth rate of that mode is significantly smaller than the growth that occurs in Crow's forced solution (see discussion of Leib, Wundrow & Goldstein 1999, below).

Crow's analysis breaks down when the downstream distance becomes $O(\lambda\ell)$, where $\ell = \min\{R_\lambda, \epsilon^{-1}\}$, at which point spanwise-diffusion or nonlinear effects (or both) become important. The near-surface flow is then determined by a slightly simplified version of the full Navier–Stokes equations, namely the Navier–Stokes equations with the streamwise derivatives neglected in the viscous and pressure-gradient terms. Kemp (1951), who first introduced these equations, referred to them as the boundary-region equations, and we shall adopt this terminology here. Goldstein† & Wundrow (1998) and Goldstein (1997) used these equations to investigate the response of laminar boundary layers to free-stream disturbances and thereby extended the original Crow (1966) analysis to include cross-stream ellipticity and nonlinear effects. An important purpose of the present paper is to provide detailed numerical confirmation of several conjectures that appear in this earlier work.

The boundary-region equations can be linearized about the Blasius solution when $r \ll 1$ and the linearized equations have recently been applied to the free-stream disturbance problem by a number of investigators. Andersson, Berggren & Henningson (1999) and Luchini (2000, in a follow-on to his 1996 paper which dealt only with solutions to the linearized boundary-*layer* equations) computed optimal spatial growth rates for steady perturbations which were introduced near the leading edge but vanish in the free stream. Bertolotti (1997) used the linearized boundary-region equations to compute the evolution of a quasi-self-similar disturbance introduced downstream of the leading edge and subjected to continuous forcing by a free-stream vorticity mode. Despite the differences in initial and boundary conditions, these computations produced normalized fluctuating streamwise velocity profiles that are in remarkably good agreement with the experimental findings. This somewhat surprising result is a consequence of the fact that almost any cross-flow perturbation introduced into the boundary layer will develop into a streamwise streak through the so-called lift-up effect (Landahl 1977). The streak then leads to a thickening and thinning of the

† The material was originally presented at the international conference in honour of Sir James Lighthill held at Florida State University in November 1996.

boundary layer with a very universal streamwise velocity profile that is reasonably well described by the formula originally derived by Taylor (1939).

A much more difficult challenge is the prediction of the streamwise growth of the Klebanoff modes. The aforementioned analyses did not properly match the boundary-region solutions onto the incident free-stream disturbances and could therefore only compare the computed and measured streamwise-velocity growth in an *ad hoc* fashion. The appropriate matching was worked out by Leib *et al.* (1999) who represented the free-stream turbulence by a superposition of vortical Fourier modes and determined the response in the boundary layer by computing the corresponding Fourier-component solutions to the linearized boundary-region equations. The results were then superposed to compute the root mean square of the fluctuating streamwise velocity in the boundary layer produced by the actual free-stream turbulence.

The Leib *et al.* (1999) calculations show that continuous forcing is essential for producing the large Klebanoff-mode growth rates actually observed in the experiments even in the downstream region where the Crow (1966) analysis breaks down. They also show that Klebanoff-mode growth exhibits a strong sensitivity to low-frequency anisotropy in the free-stream turbulence spectrum – a result which could not have been obtained if the boundary-region solutions had not been required to match onto the incident free-stream disturbance. Finally, it is worth noting that Leib *et al.* (1999) as well as Choudhari (1996) did not have to include the eigenmode solutions of Luchini (1996) in order to match their perturbed boundary-layer flows onto vortical disturbances in the free stream, which suggests that these eigensolutions would not be generated by an incident free-stream turbulence field. The present work shows that this is also true in the nonlinear case.

The statistical analysis of Leib *et al.* (1999) provides results that can be compared with experiment but, for reasons given below, the transition process can only be explained by including nonlinearity from the outset and considering the instantaneous velocity profiles. Then since the experiments show that the Klebanoff modes are of very low frequency and the Leib *et al.* (1999) analysis (also see Gulyaev *et al.* 1989) shows that they are driven only by the cross-flow components of the free-stream velocity, *an appropriate canonical problem that captures the correct physics might be the flow over a flat plate due to a steady streamwise vorticity distribution imposed on an otherwise uniform stream.* The Crow (1966) analysis is of this type but, as indicated above, it eventually breaks down at downstream distances of $O(\lambda\ell)$ which is equal to $O(\lambda\epsilon^{-1})$ when the disturbance Reynolds number is large, i.e. $r \gg 1$. Nonlinear effects then become important while spanwise-diffusion and cross-flow-ellipticity effects remain negligible. The large-r limit was considered by Goldstein & Leib (1993, hereafter referred to as GL). This was based on earlier work by Goldstein, Leib & Cowley (1992) who carried out a similar analysis for the case where the upstream vorticity was normal to plate surface.

The GL analysis shows that the cross-flow effects produce order-one changes in the streamwise boundary-layer velocity profiles at $O(\lambda\epsilon^{-1})$ distances from the leading edge which means that the boundary-layer flow is then fully three dimensional. The linear rapid-distortion-theory solution, which was shown to describe the interaction of the upstream disturbance with the leading edge, also breaks down at these downstream distances. The inviscid flow outside the boundary layer is then governed by the two-dimensional, time-dependent vorticity equation with the streamwise coordinate playing the role of the time. The entire flow field is therefore nonlinear in this stage, but remains parabolic in the streamwise direction.

The GL analysis also shows that the resulting external cross-stream pressure

gradients eventually cause the three-dimensional boundary layer to break down due to a so-called collisional-type separation (Cebeci, Khattab & Stewartson 1981). The breakdown is preceded by a highly localized (in the spanwise direction) thickening of the boundary layer as increasing amounts of low-momentum near-wall fluid are advected toward the boundary-layer edge. This nonlinear behaviour might explain the so-called 'backward jets' which were identified as precursors to turbulent-spot formation in some recent direct numerical simulations of the effect of free-stream turbulence on boundary-layer transition (Wu *et al.* 1999; Jacobs & Durbin 2001). GL found that the streamwise velocity profiles become inflectional prior to breakdown and suggested that these profiles could become unstable to Rayleigh-type instabilities thereby providing a mechanism for turbulent-spot formation closer to the wall.

Most of the more recent experimental studies of the effect of free-stream turbulence on pre-transitional boundary layers (e.g. Roach & Brierley 1992; Blair 1992; Westin *et al.* 1994; Kendall 1998) were carried out at moderate values of the disturbance Reynolds number – typically less than 100 or so. The present paper therefore reconsiders the flow analysed in GL in the more general context where the disturbance Reynolds number is order one, i.e. $r = O(1)$. The Crow (1966) analysis still breaks down at downstream distances of $O(\lambda\epsilon^{-1})$ in this limit but now with spanwise-diffusion, cross-flow-ellipticity and nonlinear effects all coming into play. The flow in the vicinity of the leading edge can still be linearized and remains unchanged at lowest approximation, but the downstream nonlinear inviscid region and corresponding three-dimensional boundary layer merge into a single region in which the flow is governed by the full nonlinear boundary-region equations.

The relation of Klebanoff modes to boundary-layer transition has been somewhat contentious over the years. The experimental evidence as well as the results of the recent numerical simulations of Jacobs & Durbin (2001) suggest that the connection can be found by considering the nonlinear stage of the instantaneous velocity profiles as originally pointed out by Goldstein & Wundrow (1998). They showed that nonlinear focusing effects can produce large localized distortions of the flow even when the spanwise-average velocity distortion (which is the one usually reported by the experimenters) is relatively small. The localized distortions tend to develop distinct shear layers which are remarkably similar to the ones observed by Kovasznay, Komoda & Vasudeva (1962) for Tollmien–Schlichting-wave type transitions. These shear layers tend to be highly inflectional and can therefore support rapidly growing instabilities that are believed to break down into turbulent spots (see Greenspan & Benney 1963). This suggests that the ultimate breakdown into turbulence depends on localized features of the flow and not on the average conditions usually reported in the Klebanoff-mode experiments.

The primary purpose of the present paper is to use accurate numerical computations to further investigate this possibility. Then, as indicated above, it is not unreasonable to begin with a steady cross-stream distortion in the upstream flow. The computed results show that two regions of enhanced instability can emerge as the boundary-layer velocity profiles become sufficiently nonlinear. The first region appears relatively close to the wall while the second lies in the outer reaches of the boundary layer. Both are highly localized in the spanwise direction and involve highly inflectional streamwise velocity profiles which can support Rayleigh-type instabilities. These instabilities grow on a streamwise length scale that is significantly smaller than the boundary-layer thickness and can therefore easily dominate the much slower growing Tollmien–Schlichting waves – which grow on the much longer viscous scale and which are the only instability waves that would exist in the absence of the imposed streamwise

vorticity. These highly localized Rayleigh instabilities can then lead to a local transition of the boundary layer, as pointed out by Goldstein & Wundrow (1998) and as observed in the Jacobs & Durbin (2001) simulations. The resulting turbulent flow is likely to resemble a turbulent spot (Kovasznay *et al.* 1962).

Our calculations show that the strength and location of these distortions are quite sensitive to the details of the imposed upstream disturbance and that the occurrence of moderately strong distortions, which are the ones expected to undergo this breakdown process, is relatively rare. This might explain the intermittent behaviour of the experimentally observed turbulent spots. The analysis also shows that the average velocity profiles that are usually reported in the Klebanoff-mode experiments are likely to mask the strong localized distortions that produce the spots. It is therefore unlikely that these types of results, or for that matter, the corresponding root-mean-square velocity fluctuations calculated in Leib *et al.* (1999) are all that relevant to the actual transition process.

While the large-r asymptotics of GL cannot be used to qualitatively predict the results of the Klebanoff-mode experiments, they can provide a relatively simple analytical structure for understanding the basic phenomena. This structure is most easily constructed by introducing appropriate shear layers (vortex sheets) to eliminate the singularities that appear in the GL analysis. Another purpose of this paper is therefore to show how these singularities, which are associated with the collisional separation of the cross-stream flow that was described above, can be eliminated. We were able to compute solutions to the present problem for fairly large values of r. The numerical results suggest that this separated cross-flow will leave the surface to form a vortex sheet and that the viscous effects should be confined to a surface boundary layer and a viscous layer surrounding the sheet as $r \to \infty$. The slender-body analysis used by Smith (1977) and others to predict the separated flow over slender cones at a small angle of attack then suggests that the resulting infinite-disturbance Reynolds-number flow will remain parabolic in the streamwise direction and that the inviscid region will be governed by a kind of slender-body approximation, but with distributed vorticity throughout the flow. The streamwise velocities computed below show no evidence of separation in the usual sense but the cross-flow profiles exhibit a strong tendency to break away from the surface. This phenomenon is sometimes referred to as cross-flow separation in the literature. It should be emphasized that true vortex sheets only form in the infinite-disturbance Reynolds-number limit, but our computations show that the finite-disturbance Reynolds-number solutions approach this behaviour as r becomes large.

The turbulent-spot-formation mechanisms described above are most likely to occur for free-stream turbulence levels in the range 0.1–5%. For turbulence levels below 0.1%, transition results from the orderly amplification of nearly discrete-frequency, two-dimensional, Tollmien–Schlichting waves. These primary instabilities eventually become large enough to support oblique secondary instabilities that can then interact nonlinearly to generate strong spanwise-variable mean-flow distortions (see, for example, Benney 1984; Goldstein & Choi 1989; Hall & Smith 1991; Hall & Horseman 1991; Wu 1993; Mankbadi, Wu & Lee 1993) which are structurally similar to the Klebanoff modes discussed above. We have already indicated that the subsequent destabilization and breakdown of this flow (which was observed in the Kovasznay *et al.* 1962 experiments) should then follow the path outlined above for the Klebanoff modes. This is an example of how different initial states can ultimately lead to the same final state – which is consistent with the frequently evoked characterization of a fully developed turbulent flow as a phase-space attractor. In fact, the formation

of streaks and their subsequent breakdown due to secondary instabilities may be a universal aspect of all transition processes in the boundary layer and, in that respect, the Klebanoff modes may be thought of as a true 'bypass mechanism' that bypasses the Tollmien–Schlichting-wave stage.

The wall-layer streaks in a turbulent boundary layer, which (like the Klebanoff modes) are spanwise-variable regions of high and low streamwise velocity associated with counter-rotating streamwise vortices, may be driven by the turbulence in the outer part of the boundary layer in the same way that Klebanoff modes are driven by free-stream turbulence (Kline *et al.* 1967). However, the effective disturbance Reynolds number might be significantly larger in this case, so that significant cross-flow separation might occur – corresponding to the experimentally observed ejections in the fully turbulent boundary layer. The present work would then suggest that these ejections are the result of a collisional-type boundary-layer separation similar to the one that occurs on slender cones at an angle of attack to the incoming flow.

Cantwell, Coles & Dimotakis (1978) observed elongated streamwise disturbances in the wall region below growing turbulent spots. They conjectured that these were Taylor–Görtler vortices generated by the passage of the spot. A more likely scenario is that they are driven by the turbulence within the spot in the same way as the Klebanoff modes are driven by the free-stream turbulence.

The phenomena being considered in this paper are therefore quite generic. In fact, it is worth noting that one of the suggestions arising from the *Workshop on Coherent Structure of Turbulent Boundary Layers* (Smith & Abbott 1979) was that the dynamics of counter-rotating vortices should be the subject of a detailed study. We believe that the present work significantly contributes to that objective.

The problem is formulated in §2 where the upstream linearized solution is discussed. The boundary-region and vortical-free-stream problems that match onto this solution are discussed in §3. These problems are, in general, coupled when formulated in terms of primitive variables, but, as shown in §3, the free-stream problem can be completely decoupled from the boundary-region problem that applies near the surface of the plate by introducing appropriately transformed variables into the governing equations. This allows the corresponding solutions to be found *seriatum* and greatly simplifies the numerical computation. The numerical method used to solve the boundary-region problem is described in §4. The numerical results are presented in §5, and their implications for turbulent-spot formation and other issues related to sublayer streaks are discussed.

2. Formulation and breakdown of the linear solution

As in GL, attention is focused on an incompressible flow over a semi-infinite flat plate due to a small, $O(\epsilon)$, streamwise vorticity field, with characteristic length scale λ, imposed on an otherwise uniform upstream flow. All lengths are non-dimensionalized by λ, the velocity $\boldsymbol{u} = \{u, v, w\}$ is non-dimensionalized by the uniform upstream velocity U_∞, and the pressure is non-dimensionalized by ρU_∞^2, where ρ is the (constant) density. The Cartesian coordinate system $\{x, y, z\}$ is placed at the leading edge of the plate with x in the direction of the undisturbed free stream, y normal to the plate, and z along the span.

It follows that

$$\boldsymbol{u} \to \boldsymbol{i} + \epsilon \left(\boldsymbol{j}\psi_{\infty z} - \boldsymbol{k}\psi_{\infty y} \right) \quad \text{as} \quad x \to -\infty, \tag{2.1}$$

where $\psi_\infty(y, z)$ is a cross-flow stream function used to characterize the upstream disturbance, $\{\boldsymbol{i}, \boldsymbol{j}, \boldsymbol{k}\}$ are unit vectors in the $\{x, y, z\}$ directions, respectively, and an

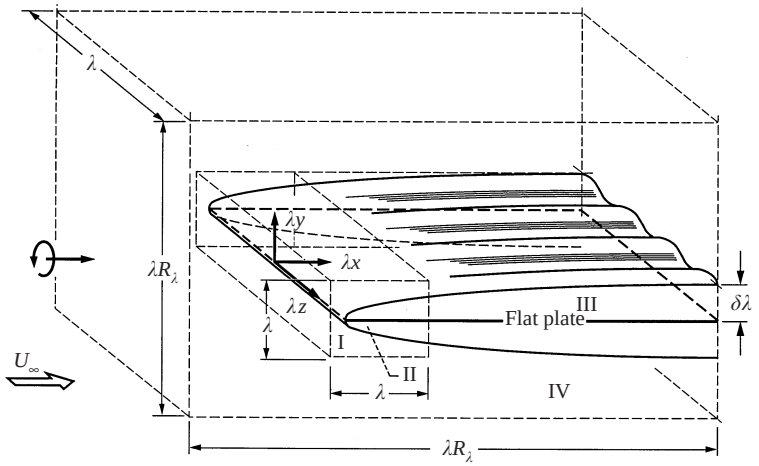

FIGURE 1. Flow configuration.

independent variable used as a subscript denotes differentiation with respect to that quantity.

The effects of plate thickness are largely irrelevant for the imposed streamwise vorticity fields being considered herein; so, for simplicity, the plate is taken to be infinitely thin. As in GL, the Reynolds number $R_\lambda \equiv \lambda U_\infty/\nu$, where ν is the kinematic viscosity, is assumed to be large enough so that viscous effects are initially confined to a thin layer near the plate surface. However, as indicated in §1, it is now assumed that

$$r \equiv \epsilon R_\lambda = \epsilon\lambda U_\infty/\nu = 1/\sigma = O(1), \tag{2.2}$$

where σ is introduced in order to simplify the equations.

Then in the limit as $\epsilon \to 0$ and $R_\lambda \to \infty$ with r (or σ) held fixed at $O(1)$, the flow divides itself into the four distinct asymptotic regions shown in figure 1. The GL analysis corresponds, at least in part, to the $r \to \infty$ limit of the present result (see Appendix B). The low-turbulence Reynolds-number analysis of Leib *et al.* (1999) is a generalization (to include unsteady effects) of the $r \to 0$ limit of the present result, and the general case is discussed in Goldstein (1997) and Goldstein & Wundrow (1998).

The flow in region I, which is a basically inviscid region of dimensions $O(\lambda)$, is governed by linear rapid-distortion theory. Beneath this region is a predominantly viscous layer, denoted region II in figure 1, in which the flow is nearly two-dimensional, with three-dimensional effects entering only as an $O(\epsilon)$ perturbation to the Blasius solution. But as indicated by Crow (1966), the boundary-layer displacement effects induce an $O(\epsilon^{1/2})$ correction to the rapid-distortion solution when σ is $O(1)$. This is most easily accounted for by expanding the inviscid solution in region I (where x and y are both $O(1)$) as

$$\boldsymbol{u} = \nabla\Phi + \epsilon\boldsymbol{u}_0 + \epsilon^2\boldsymbol{u}_1 + \cdots, \tag{2.3}$$

$$p = -\tfrac{1}{2}|\nabla\Phi|^2 + \epsilon p_0 + \epsilon^2 p_1 + \cdots, \tag{2.4}$$

and including the displacement effects in the base-flow potential $\Phi(x, y)$. Then (cf. Van Dyke 1975),

$$\Phi = x - \mathrm{Re}\,\mathrm{i}\beta(2\sigma\epsilon\xi)^{1/2} + \cdots, \tag{2.5}$$

to the required order of accuracy, and $\{\boldsymbol{u}_n, p_n\}$ include terms of $O(\epsilon^{1/2})$ where Re

denotes the real part, $\mathrm{i} \equiv (-1)^{1/2}$, $\xi \equiv x + \mathrm{i}y$, and β is a constant determined by the Blasius solution (see (2.15) below).

The $O(\epsilon)$ terms in (2.3) and (2.4) are governed by the linearized Euler equations; so the results of Goldstein (1978) can be used to write

$$\boldsymbol{u}_0 = \{u_0, v_0, w_0\} = \nabla\phi + \boldsymbol{u}^{(I)}, \tag{2.6}$$

$$p_0 = -\nabla\Phi \cdot \nabla\phi, \tag{2.7}$$

where (Kerschen & Balsa 1981)

$$\boldsymbol{u}^{(I)} = \left(\nabla\Psi \frac{\partial}{\partial z} - \boldsymbol{k}\frac{\partial}{\partial \Psi}\right) \psi_\infty(\Psi, z), \tag{2.8}$$

the base-flow stream function $\Psi(x, y)$ is given by

$$\Psi = y - \mathrm{Re}\,\beta(2\sigma\epsilon\xi)^{1/2}, \tag{2.9}$$

and the perturbation potential $\phi(x, y, z)$ satisfies

$$\nabla^2\phi = -\nabla \cdot \boldsymbol{u}^{(I)} \tag{2.10}$$

subject to

$$\phi \to 0 \quad \text{as} \quad x \to -\infty, \quad \nabla\phi \to 0 \quad \text{as} \quad y \to \pm\infty, \quad \phi = 0 \quad \text{at} \quad y = 0,\ x < 0, \tag{2.11}$$

and an appropriate matching condition on $\Psi = 0$, $x > 0$. To lowest order of approximation, the matching condition simply requires that the normal velocity v_0 vanish at the surface of the plate. This does not, however, determine ϕ correct to $O(\epsilon^{1/2})$, which is necessary in order to derive upstream conditions that are accurate enough to start the numerical solution in region III.

The complete solution to (2.10) and (2.11) can be found using the Wiener–Hopf technique (Noble 1958) once the appropriate boundary condition on $\Psi = 0$ has been specified. The relevant result has a 'square root' singularity at the leading edge of the plate, which, however, has no affect on the solution in region III, which is of primary interest here, because the singular part of ϕ decays exponentially fast as $x \to \infty$ (Choudhari 1996). GL show that the lowest-order flow in region I eventually becomes two-dimensional in the cross-flow plane at large downstream distances, and Crow's (1966) results can then be used to express the velocity field in region II as

$$u = F' + \epsilon w_{0z}(x, 0, z)\tfrac{1}{2}x\eta F'' + \cdots, \tag{2.12}$$

$$v = \epsilon\sigma\Delta^{-1}(\eta F' - F) + \epsilon w_{0z}(x, 0, z)\tfrac{1}{4}\Delta G + \cdots, \tag{2.13}$$

$$w = \epsilon w_0(x, 0, z)F' + \cdots, \tag{2.14}$$

when x is in the overlap region $1 \ll x \ll \epsilon^{-1}$. Here $\Delta \equiv (2\sigma\epsilon x)^{1/2}$, $\eta \equiv y/\Delta = O(1)$, the Blasius function $F(\eta)$ satisfies

$$F''' + FF'' = 0, \quad F(0) = F'(0) = 0, \quad F \to \eta - \beta \quad \text{as} \quad \eta \to \infty, \tag{2.15}$$

$G(\eta) \equiv \eta^2 F'' - 3\eta F' - F$, a prime denotes differentiation with respect to the argument and $w_0(x, 0, z)$ denotes the spanwise velocity component of the zeroth-order rapid-distortion solution evaluated at the surface of the plate. In view of (2.6) and (2.8)–(2.11), w_0 must expand like

$$w_0(x, 0, z) = w_{00}(0, z) + \Delta w_{01}(0, z) + \cdots,$$

for $1 \ll x \ll \epsilon^{-1}$, (see (2.21) below).

The $\Psi = 0$ boundary condition for ϕ can now be determined to the required order of accuracy in the overlap region by matching the large-η expansions of (2.12)–(2.14) with the small-Ψ expansion of (2.3), which yields

$$\phi_y + v^{(I)} = \tfrac{1}{4}\beta\Delta(\phi_{zz} + w_z^{(I)}) \quad \text{at} \quad y = 0, \tag{2.16}$$

where use has been made of (2.6), (2.10) and the requirement that $1 \ll x \ll \epsilon^{-1}$.

Since the analysis is restricted to smooth spanwise-periodic imposed vorticity fields, ψ_∞ can be expressed in terms of a Fourier series of the form

$$\psi_\infty = \sum_{m=-\infty}^{+\infty} \psi_\infty^{(m)}(y)\, \mathrm{e}^{\mathrm{i}\gamma m z}, \tag{2.17}$$

where $\psi_\infty^{(0)}(y) = 0$, $m^2\psi_\infty^{(m)}(y) \to 0$ as $|m| \to \infty$, and similarly for ϕ. The scale factor γ is determined such that the non-dimensional characteristic length of the imposed disturbance is unity (see (5.6) below). Substituting (2.17) and the corresponding expression for ϕ into (2.8), (2.10), (2.11) and (2.16) and equating like powers of $\mathrm{e}^{\mathrm{i}z}$ yields a system of boundary-value problems in y which can be solved to show that

$$\phi^{(m)} = \mathrm{i}\frac{m}{|m|}\left\{\psi_\infty^{(m)}(0) - \tfrac{3}{4}\beta\Delta\left[\psi_\infty^{(m)\prime}(0) + \gamma|m|\psi_\infty^{(m)}(0)\right]\right\}\mathrm{e}^{-\gamma|m|y^*}, \tag{2.18}$$

to the required order of accuracy for $1 \ll x \ll \epsilon^{-1}$, where the shifted coordinate

$$y^* = y - \beta\Delta \tag{2.19}$$

accounts for the displacement thickness of the Blasius flow.

It therefore follows from (2.5)–(2.9), (2.17) and (2.18) that the $O(\epsilon)$ terms in (2.3) and (2.4) can be written as

$$v_0 = \psi_{0z}(y^*, z) - \beta\Delta\pi_{0yz}(y, z) + \cdots, \tag{2.20}$$

$$w_0 = -\psi_{0y^*}(y^*, z) + \beta\Delta\pi_{0yy}(y, z) + \cdots, \tag{2.21}$$

$$p_0 = \epsilon\sigma\beta\Delta^{-1}\pi_{0z}(y, z) + \cdots, \tag{2.22}$$

when x is in the overlap region, where

$$\psi_0(y, z) \equiv \sum_{m=-\infty}^{+\infty}\left[\psi_\infty^{(m)}(y) - \psi_\infty^{(m)}(0)\mathrm{e}^{-\gamma|m|y}\right]\mathrm{e}^{\mathrm{i}\gamma m z}, \tag{2.23}$$

$$\pi_0(y, z) \equiv \tfrac{3}{4}\sum_{m=-\infty}^{+\infty}\frac{1}{\gamma|m|}\left[\psi_\infty^{(m)\prime}(0) + \gamma|m|\psi_\infty^{(m)}(0)\right]\mathrm{e}^{-\gamma|m|y + \mathrm{i}\gamma m z}. \tag{2.24}$$

It is now clear that the boundary-layer displacement effects cause the solution (2.18) to break down when x is $O(\epsilon^{-1})$, which reflects the fact that the viscous-diffusion effects become important on an $O(1)$ y-scale. Moreover, GL show that nonlinear effects also become important when x is $O(\epsilon^{-1})$ and cause a further disordering of the expansions (2.3) and (2.4). A new solution must therefore be constructed in region III where y and

$$\bar{x} \equiv \epsilon x \tag{2.25}$$

are both $O(1)$.

3. The nonlinear boundary-region problem

Introducing the scaled streamwise variable (2.25) into (2.12)–(2.14) shows that the velocity field in this nonlinear viscous region should expand like

$$u = U(\bar{x}, y, z) + \cdots, \quad v = \epsilon V(\bar{x}, y, z) + \cdots, \quad w = \epsilon W(\bar{x}, y, z) + \cdots, \tag{3.1}$$

while (2.4), (2.5) and (2.22) imply that the corresponding pressure field expands like

$$p = -\tfrac{1}{2} + \epsilon^2 P(\bar{x}, y, z) + \cdots. \tag{3.2}$$

Substituting these results, together with (2.2) and (2.25), into the full Navier–Stokes equations and equating like powers of ϵ yields the boundary-region equations of Kemp (1951)

$$U_{\bar{x}} + V_y + W_z = 0, \tag{3.3}$$

$$UU_{\bar{x}} + VU_y + WU_z = \sigma(U_{yy} + U_{zz}), \tag{3.4}$$

$$UV_{\bar{x}} + VV_y + WV_z + P_y = \sigma(V_{yy} + V_{zz}), \tag{3.5}$$

$$UW_{\bar{x}} + VW_y + WW_z + P_z = \sigma(W_{yy} + W_{zz}). \tag{3.6}$$

Like the three-dimensional, boundary-layer equations, which describe the flow in the corresponding region in GL, these equations are parabolic in the streamwise direction, but they are now elliptic, rather than hyperbolic, in the cross-flow plane.

The solutions to (3.3)–(3.6) must satisfy the no-slip condition

$$U = V = W = 0 \quad \text{at} \quad y = 0, \tag{3.7}$$

and must match onto the linear solutions of §2 as $\bar{x} \to 0$. The latter condition is rather more intricate than that for the boundary-layer problem analysed in GL because the increased thickness of region III means that (3.1) and (3.2) must be matched onto the downstream limits of the solutions in both regions I and II. The details are given in Appendix A where a single set of upstream conditions is arrived at by constructing composite expansions for the velocity and pressure fields that are uniformly valid in y as $\bar{x} \to 0$.

The assumed spanwise periodicity of the imposed disturbance (2.17) implies that the boundary-region solutions must also be spanwise periodic. The boundary conditions at large transverse distances are obtained by matching to the solution in region IV. The streamwise velocity component must, of course, satisfy

$$U \to 1 \quad \text{as} \quad y \to \infty, \tag{3.8}$$

in order to match with the uniform stream. The V and W velocity components must, on the other hand, match onto an $O(\epsilon)$ cross-flow that is affected (at leading order) by the spanwise-averaged displacement thickness of the boundary-region solution, i.e.

$$\bar{\delta}(\bar{x}) \equiv \frac{\gamma}{2\pi} \int_0^{2\pi/\gamma} \int_0^{\infty} (1 - U) \mathrm{d}y \mathrm{d}z. \tag{3.9}$$

This displacement induces a two-dimensional inviscid flow in region IV where the appropriately scaled transverse variable is

$$\bar{y} \equiv \epsilon y = O(1). \tag{3.10}$$

The form of the solution is then determined by substituting (2.25) and (3.10) into (2.3)–(2.5) and recognizing that the transverse scale of the zeroth-order rapid-distortion solution is set by the imposed disturbance (2.17) which means that the $O(\epsilon)$ flow in

region IV must have a cross-flow component that depends explicitly on y as well as on the 'slow' variable $\bar{y}$ over which modulations due to the plate-induced flow effects occur. In view of this, the governing equations can be simplified by separating out the two-dimensional inviscid motion and the solution is therefore expressed as

$$u = 1 + \epsilon\,[\bar{u}_0(\bar{x}, \bar{y}) + \hat{u}_0(\bar{x}, \bar{y}, y, z)] + \cdots, \tag{3.11}$$

$$v = \epsilon\,[\bar{v}_0(\bar{x}, \bar{y}) + \hat{v}_0(\bar{x}, \bar{y}, y, z)] + \cdots, \tag{3.12}$$

$$w = \epsilon \hat{w}_0(\bar{x}, \bar{y}, y, z) + \cdots, \tag{3.13}$$

$$p = -\tfrac{1}{2} + \epsilon \bar{p}_0(\bar{x}, \bar{y}) + \epsilon^2 \hat{p}_1(\bar{x}, \bar{y}, y, z) + \cdots, \tag{3.14}$$

where $\{\bar{u}_0, \bar{v}_0, \bar{p}_0\}$ satisfies the two-dimensional Euler equations and $\{\hat{u}_0, \hat{v}_0, \hat{w}_0, \hat{p}_1\}$ must match onto the zeroth-order rapid-distortion solution as $\bar{x} \to 0$.

As $\bar{y} \to 0$, the solution for $\bar{v}_0$ must match onto the spanwise-averaged normal velocity at the edge of region III, which (unlike the remaining portion of V) is determined internally by the boundary-region flow itself. Integrating (3.3) from $z = 0$ to $2\pi/\gamma$ and then from $y = 0$ to ∞ and making use of (3.9) leads to the requirement

$$\bar{v}_0 = -\frac{\gamma}{2\pi} \int_0^{2\pi/\gamma} \int_0^{\infty} U_{\bar{x}} \mathrm{d}y \mathrm{d}z = \bar{\delta}'(\bar{x}) \quad \text{at} \quad \bar{y} = 0. \tag{3.15}$$

Then since $\{\bar{u}_0, \bar{v}_0, \bar{p}_0\}$ vanishes as $\bar{x} \to 0$, the resulting two-dimensional flow is irrotational, and it follows from complex-variable theory and the linearized Euler equations that

$$\bar{u}_0 = -\bar{p}_0 = -\mathrm{Re}\,\mathrm{i}\bar{\delta}'(\bar{\xi}), \quad \bar{v}_0 = \mathrm{Re}\,\bar{\delta}'(\bar{\xi}), \tag{3.16}$$

provided $\bar{\delta}$ can be analytically continued to complex values of $\bar{\xi} \equiv \epsilon\xi = \bar{x} + \mathrm{i}\bar{y}$.

Substituting (3.16) into (3.11)–(3.14) and the result together with (2.2) and (2.25) into the full Navier–Stokes equations and introducing the modified Prandtl transformation

$$\hat{y} \equiv y - \mathrm{Re}\,\bar{\delta}(\bar{\xi}) = O(\epsilon^{-1}), \tag{3.17}$$

to remove the explicit dependence on the plate-induced flow effects (and consequently on the slow variable $\bar{y}$) shows that the cross-flow in region IV is governed by

$$\hat{v}_{0\hat{y}} + \hat{w}_{0z} = 0, \tag{3.18}$$

$$\hat{v}_{0\bar{x}} + \hat{v}_0 \hat{v}_{0\hat{y}} + \hat{w}_0 \hat{v}_{0z} + \hat{p}_{1\hat{y}} = \sigma\left(\hat{v}_{0\hat{y}\hat{y}} + \hat{v}_{0zz}\right), \tag{3.19}$$

$$\hat{w}_{0\bar{x}} + \hat{v}_0 \hat{w}_{0\hat{y}} + \hat{w}_0 \hat{w}_{0z} + \hat{p}_{1z} = \sigma\left(\hat{w}_{0\hat{y}\hat{y}} + \hat{w}_{0zz}\right), \tag{3.20}$$

which, in order to match with (2.23), must be solved subject to

$$\hat{v}_0 = \psi_{\infty z}(\hat{y}, z), \quad \hat{w}_0 = -\psi_{\infty\hat{y}}(\hat{y}, z) \quad \text{at} \quad \bar{x} = 0. \tag{3.21}$$

Equations (3.16)–(3.20) then show that streamwise ellipticity, which is the new feature in region IV, only affects the two-dimensional flow $\{\bar{u}_0, \bar{v}_0, \bar{p}_0\}$ and that the governing equations for $\{\hat{v}_0, \hat{w}_0, \hat{p}_1\}$ remain parabolic in $\bar{x}$ when written in terms of $\hat{y}$. Equations (3.18) and (3.21) along with the assumed form of the imposed disturbance (2.17) show that the spanwise average of $\hat{v}_0$ is identically zero for all $\bar{x}$. The same is not, in general, true of the spanwise averages of $\hat{w}_0$ and $\hat{p}_1$.

Equating the outer limits of (3.1) and (3.2) with the inner limits of (3.11)–(3.14) and making use of (3.16) yields the matching conditions

$$U \to 1, \tag{3.22}$$

$$V \to \bar{\delta}'(\bar{x}) + \hat{v}_0(\bar{x}, y - \bar{\delta}, z), \tag{3.23}$$

$$W \to \hat{w}_0(\bar{x}, y - \bar{\delta}, z), \tag{3.24}$$

$$P \to \hat{p}_1(\bar{x}, y - \bar{\delta}, z), \tag{3.25}$$

as $y \to \infty$. Equations (3.23)–(3.25) clearly show that the disturbance-induced cross-flow in region IV gives rise to a continuous forcing of the boundary-region problem.

The spanwise periodicity of the imposed disturbance (2.17) implies that the solution in region IV must also be spanwise periodic. Furthermore, since (3.22)–(3.25) place no restrictions on the solution to (3.18)–(3.20), it follows from (3.17) and (3.21) that the transverse boundary conditions only depend on the large-y behaviour of the imposed disturbance. Thus, one can require that $\{\hat{v}_0, \hat{w}_0, \hat{p}_1\}$ be periodic in $\hat{y}$ when the imposed upstream disturbance is periodic in y and similarly when the imposed disturbance is a stationary random function of that variable. This completes the specification of the boundary-value problem for the cross-flow in region IV which can now be solved (in terms of $\hat{y}$) independently of the boundary-region solution because the latter enters the former only through the transformation (3.17). The solution in region IV can therefore be found before determining the solution in region III and the result can then be used to obtain the appropriate outer-edge boundary conditions for the latter region. This allows us to greatly simplify the numerical procedure described in §4. It is worth noting here that a slightly more general form of the transformation (3.17) can be used to accomplish a similar decoupling between the unsteady versions of the region III and IV problems.

Equations (3.18)–(3.20) are just the two-dimensional, time-dependent Navier–Stokes equations with $\bar{x}$ playing the role of the time. They can therefore be reduced to a single equation in the usual way by using (3.18) to introduce a stream function $\hat{\psi}_0$ and eliminating the pressure between (3.19) and (3.20) to obtain

$$\left(\frac{\partial}{\partial \bar{x}} + \hat{\psi}_{0z}\frac{\partial}{\partial \hat{y}} - \hat{\psi}_{0\hat{y}}\frac{\partial}{\partial z}\right)\nabla_\perp^2 \hat{\psi}_0 = \sigma \nabla_\perp^4 \hat{\psi}_0, \tag{3.26}$$

where $\nabla_\perp^2$ denotes the Laplacian in the cross-flow plane. The relevant boundary-value problem can be solved numerically by using appropriate spectral approximations in the $\hat{y}$- and z-directions to reduce (3.26) to a coupled system of first-order ordinary-differential equations in $\bar{x}$ which can then be integrated using a standard Runge–Kutta algorithm. However, the result of such a computation only applies when the 'fast' variable y is much greater than one, i.e. when the distance from the plate is large compared to the spanwise length scale λ. But, as shown above, this is all that is required, since the flow is given by the boundary-region solution when y is $O(1)$.

It is easy to see that (3.26) has an exact solution of the form

$$\hat{\psi}_0 = \psi_\infty(\hat{y}, z)\mathrm{e}^{-c\sigma\bar{x}} \tag{3.27}$$

(where c is a positive constant) if ψ_∞ satisfies $\nabla_\perp^2 \psi_\infty = -c\psi_\infty$. This solution is also a solution to the corresponding linearized problem although it may not represent a stable solution.

4. Numerical solution to the boundary-region problem

The numerical solution to the boundary-region problem is obtained by decomposing the dependent variables into spanwise-averaged and spanwise-varying components

as follows:

$$\{U, V, W, P\} = \{\overline{U}, \overline{V}, \overline{W}, \overline{P}\}(\bar{x}, y) + \{\tilde{U}, \tilde{V}, \tilde{W}, \tilde{P}\}(\bar{x}, y, z), \tag{4.1}$$

where the spanwise average of $\{\tilde{U}, \tilde{V}, \tilde{W}, \tilde{P}\}$ is identically zero. Substituting (4.1) into (3.3)–(3.6) leads to the coupled system

$$\overline{U}_{\bar{x}} + \overline{V}_y = 0, \quad \mathrm{D}\overline{U} = \overline{R}_1, \quad \mathrm{D}\overline{W} = \overline{R}_3, \tag{4.2}$$

and

$$\left.\begin{aligned} \tilde{U}_{\bar{x}} + \tilde{V}_y + \tilde{W}_z = 0, \quad \mathrm{D}\tilde{U} - \overline{U}_{\bar{x}}\tilde{U} - \overline{U}_y\tilde{V} = \tilde{R}_1, \\ \mathrm{D}\tilde{V} - \overline{V}_{\bar{x}}\tilde{U} - \overline{V}_y\tilde{V} - \tilde{P}_y = \tilde{R}_2, \quad \mathrm{D}\tilde{W} - \overline{W}_{\bar{x}}\tilde{U} - \overline{W}_y\tilde{V} - \tilde{P}_z = \tilde{R}_3, \end{aligned}\right\} \tag{4.3}$$

where

$$\mathrm{D} \equiv \sigma\left(\frac{\partial^2}{\partial y^2} + \frac{\partial^2}{\partial z^2}\right) - \overline{U}\frac{\partial}{\partial \bar{x}} - \overline{V}\frac{\partial}{\partial y} - \overline{W}\frac{\partial}{\partial z}, \tag{4.4}$$

accounts for viscous diffusion in the cross-flow plane, as well as convection by the spanwise-averaged flow field, and the nonlinear right-hand sides are given by

$$\begin{aligned} \{R_1, R_2, R_3\} &= \{\overline{R}_1, \overline{R}_2, \overline{R}_3\}(\bar{x}, y) + \{\tilde{R}_1, \tilde{R}_2, \tilde{R}_3\}(\bar{x}, y, z) \\ &\equiv \left(\tilde{U}\frac{\partial}{\partial \bar{x}} + \tilde{V}\frac{\partial}{\partial y} + \tilde{W}\frac{\partial}{\partial z}\right)\{\tilde{U}, \tilde{V}, \tilde{W}\}. \end{aligned} \tag{4.5}$$

The spanwise-averaged component of the normal momentum equation is not included with (4.2) because it is not coupled to the other equations and serves only to determine the (passive) spanwise-averaged pressure $\overline{P}$.

It follows from (3.7), (3.22)–(3.25) and (A 1)–(A 8) that the relevant boundary conditions are

$$\overline{U} \to F', \quad \overline{V} \to \sigma\Delta^{-1}\left(\eta F' - F\right), \quad \overline{W} \to 0, \quad \text{as} \quad \bar{x} \to 0, \tag{4.6}$$

$$\overline{U} = \overline{V} = \overline{W} = 0 \quad \text{at} \quad y = 0, \quad \overline{U} \to 1, \quad \overline{W} \to \bar{w}_0(\bar{x}, y - \bar{\delta}, z) \quad \text{as} \quad y \to \infty, \tag{4.7}$$

and

$$\tilde{U} \to -\psi_{0_{yz}}(0, z)\tfrac{1}{2}\bar{x}\eta F'' + \bar{x}\Delta U_c(\eta, z), \tag{4.8}$$

$$\tilde{V} \to \psi_{0_z}(y, z) - \Delta\left[\psi_{0_{yz}}(0, z)\tfrac{1}{4}(G + 4\eta - \beta) + \beta\varphi_{yz}(y, z)\right], \tag{4.9}$$

$$\tilde{W} \to -\psi_{0_y}(y, z) + \psi_{0_y}(0, z)(1 - F') + \Delta\left[\beta\varphi_{yy}(y, z) + W_c(\eta, z)\right], \tag{4.10}$$

$$\tilde{P} \to \sigma\beta\Delta^{-1}\pi_{0_z}(y, z), \tag{4.11}$$

as $\bar{x} \to 0$,

$$\tilde{U} = \tilde{V} = \tilde{W} = 0 \quad \text{at} \quad y = 0, \tag{4.12}$$

$$\{\tilde{U}, \tilde{V}, \tilde{W}, \tilde{P}\} \to \{0, \tilde{v}_0, \tilde{w}_0, \tilde{p}_1\}(\bar{x}, y - \bar{\delta}, z) \quad \text{as} \quad y \to \infty, \tag{4.13}$$

where $\Delta = (2\sigma\bar{x})^{1/2}$, $\varphi = \psi_0 + \pi_0$, (4.8)–(4.11) are arrived at by combining (A 1)–(A 4) and (A 5)–(A 8) to form an (additive) composite expansion (Van Dyke 1975) and the spanwise-averaged displacement thickness $\bar{\delta}$ is given in terms of $\overline{U}$ by (3.9). The higher-order terms U_c and W_c, which are given in Appendix A, had to be included in order to start the computation successfully. The bar and tilde accents on $\{v_0, w_0, p_1\}$ are used in (4.7) and (4.13) to denote the spanwise-mean and varying components of the region IV cross-flow, respectively. The absence of a large-y boundary condition for $\overline{V}$ reflects the boundary-layer nature of (4.2).

A marching procedure, based on second-order-accurate backward differences for

the left-hand sides of (4.2) and (4.3) and a second-order predictor–corrector scheme for the right-hand sides, was used to advance the solution in the streamwise direction. The solution's spanwise variation was approximated by using the truncated Fourier series

$$\tilde{U} = \sum_{m=-M}^{+M} \tilde{U}^{(m)}(\bar{x}, y)\mathrm{e}^{\mathrm{i}ymz}, \tag{4.14}$$

where $\tilde{U}^{(0)}(\bar{x}, y) = 0$, and similarly for the other dependent variables. The right-hand sides of (4.2) and (4.3), which depend only on previously computed results, were then evaluated by using fast Fourier transform methods. Aliasing errors were removed by use of the $\frac{3}{2}$-rule when the FFTs were calculated. The coordinate transformation

$$y = s(\Delta^2 + s^2)^{1/2}, \tag{4.15}$$

was used to maintain sufficient numerical resolution in the transverse direction. Derivatives with respect to s were approximated using second-order-accurate finite differences, and the pressure was computed on a grid staggered in s relative to that for the velocity components.

The resulting system of algebraic equations was solved at each streamwise station and for both the predictor and corrector steps as follows: The nonlinear inhomogeneous problem for the spanwise-averaged velocity components, (4.2), (4.6) and (4.7), was solved first by means of Newton–Raphson iteration. The results of this computation were then used on the left-hand sides of (4.3) as well as in a calculation of the spanwise-averaged displacement thickness $\bar{\delta}$. The latter quantity was needed in order to evaluate the functions $\{\tilde{v}_0, \tilde{w}_0, \tilde{p}_1\}$ of $\bar{x}$, $\hat{y}$ and z (which are provided either by a prior numerical calculation or by analytic formulae) at a given value of y as required by the boundary conditions (4.13). The problem for the spanwise-varying part of the flow field is then reduced to a block tri-diagonal system of linear inhomogeneous equations which was solved subject to (4.8)–(4.13) using a standard sparse linear system algorithm. The difference between the predicted and corrected values was checked at each node, and if less than a preset tolerance, the computation was advanced to the next streamwise station.

5. Results and discussion

5.1. *The high-disturbance Reynolds-number limit*

The most appropriate upstream disturbances for the Klebanoff-mode experiments would be periodic in the transverse variable y or, better, stationary random functions of that variable (Leib *et al.* 1999). However, our first objective is to investigate the limit of high-disturbance Reynolds number, which is best accomplished by comparing the present results with the infinite-Reynolds-number results of GL. Unfortunately they chose the imposed vorticity field to be of the form

$$\psi_\infty = \operatorname{sech} y \, \sin z, \tag{5.1}$$

primarily because it is one of the simplest spanwise-periodic functions exhibiting exponential decay away from the plane of the plate. We therefore begin by considering this type of disturbance. The resulting cross-flow streamline pattern is shown in figure 2. It corresponds to an array of counter-rotating streamwise vortices centred at the plate surface. Equations (5.1), (3.10) and (3.21) imply that the resulting velocity field is exponentially small in region IV and, therefore, that the solution need not be

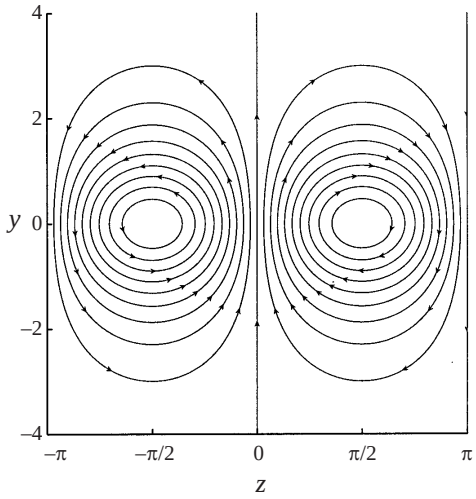

FIGURE 2. Streamline pattern in the cross-flow plane of the imposed steady upstream disturbance field (5.1).

computed in this region, since the functions $\{\tilde{v}_0, \tilde{w}_0, \tilde{p}_1\}$ appearing in (4.13), can simply be set equal to zero. This is similar to the free-stream behaviour assumed in the linear analyses of Andersson *et al.* (1999) and Luchini (2000). The lowest-order upstream flow in regions I and II is the same as in GL, and it is therefore only necessary to discuss the solution in region III.

Figure 3 shows the contours of constant streamwise velocity in the cross-flow plane at the indicated streamwise positions for a disturbance Reynolds number r of 500. They show that the solution initially behaves linearly, and the profiles have the same spanwise harmonic dependence as the imposed upstream distortion. But nonlinear effects eventually come into play, and a strong focusing occurs along the planes of maximum boundary-layer thickness. Figure 4 is a smoke-flow visualization photograph taken by Kendall (1985) which shows the flow in the cross-flow plane. The camera is placed downstream of the test section, and the smoke wire is placed at a distance above the surface of the plate corresponding to one Blasius η value. This result suggests that nonlinear focusing occurs in the experiment as well as in the theory.

Since the boundary-layer thickness (99% definition) of the undisturbed Blasius flow corresponds to $\eta \approx 3.5$, the contours in figure 3 clearly show that low-momentum fluid is eventually ejected well into the main stream when r becomes sufficiently large. This is due to cross-flow advection which can best be seen by looking at the projections of the streamlines on the cross-flow plane shown in figure 5. They suggest that well-defined shear layers will form at the surface of the plate and then roll up into a kind of spiral as they move downstream. Figure 5 also shows a secondary vortex system forming at the surface of the plate. When interpreting figure 5, it should be born in mind that continuity is not satisfied in the cross-flow plane and velocity scale can therefore not be inferred from the separation of adjacent streamlines.

Figure 6 is a three-dimensional rendering of the anticipated separation surface for the infinite-r limit. It does not show the secondary vortex system. Notice that the ordinate is η and not y in figures 3 and 5 so that the vertical scale is expanding with increasing downstream distance. This localized separation could directly lead

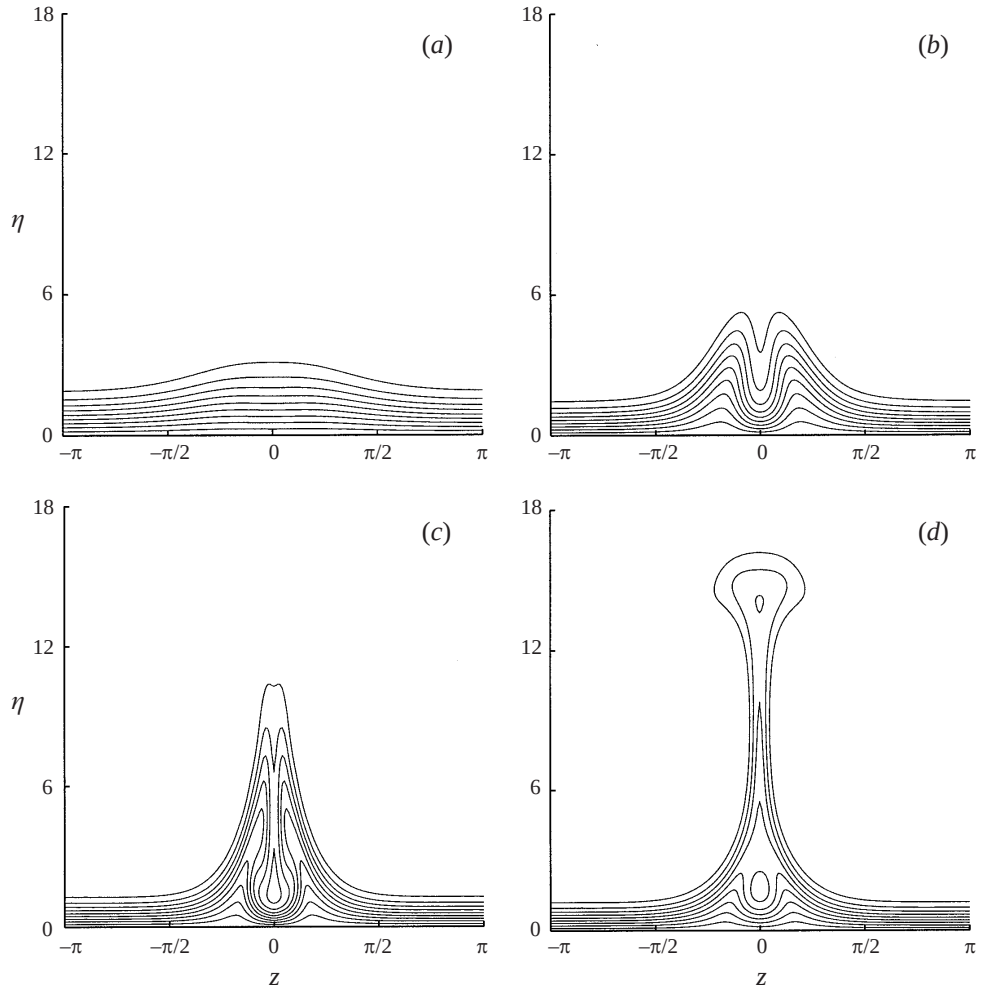

FIGURE 3. Streamwise velocity contours in the cross-flow plane for $r = 500$. (*a*) $\bar{x} = 0.6$; (*b*) $\bar{x} = 2$; (*c*) $\bar{x} = 4$; (*d*) $\bar{x} = 8$. Nine contours correspond to $U = 0.1, 0.2, \ldots, 0.9$.

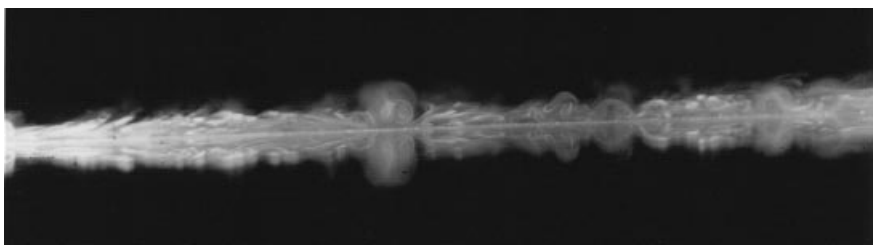

FIGURE 4. Smoke-flow visualization of boundary layer beneath a turbulent stream (from Kendall 1985).

to the formation of turbulent spots (but see below). The curves in figure 5 are in qualitative agreement with the vector plots of the streamwise velocity in the cross-flow plane shown in figure 16 of Jacobs & Durbin (2001) which suggests that nonlinear focusing also occurs in their direct numerical simulation. Better agreement would have

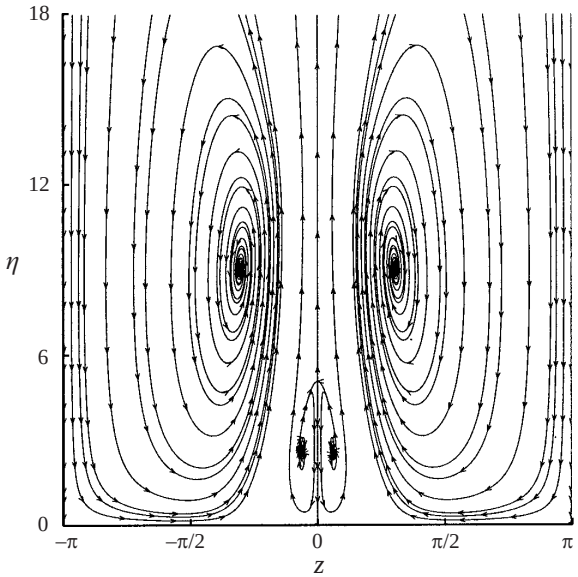

FIGURE 5. Streamline projections in the cross-flow plane for $r = 500$ and $\bar{x} = 4$.

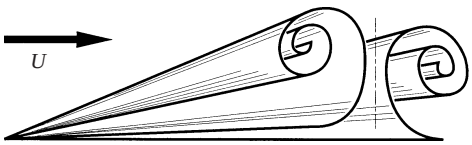

FIGURE 6. Typical separation stream surface for infinite-r solution of GL.

been obtained if comparisons were made with the more appropriate forced solutions considered in §5.2 below.

The wall-layer streaks beneath a turbulent boundary layer are elongated regions in which there are strong spanwise variations in the streamwise velocity, such as those shown in figure 3, whereas the accompanying rolls that occur in these flows may correspond to cross-flow vortices similar to those shown in figure 5. These streaks are probably driven by the turbulence in the main part of the boundary layer in the same way that the Klebanoff modes are driven by the free-stream turbulence (Kline *et al.* 1967). Figure 7 shows a pattern for the near-wall flow educed from a turbulent channel-flow calculation by Stretch (1991). This should be compared with the pattern shown in figure 6. The present analysis suggests that streaks and streamwise rolls are different aspects of the same basic flow phenomena.

The infinite-r solution of GL develops a singularity at some streamwise location and then becomes discontinuous downstream of that point. The present results suggest that the singularity can be eliminated by allowing the nonlinear inviscid solution of GL to be discontinuous across an appropriate stream surface. However, the separated flow remains parabolic in the streamwise direction and is, in fact, a generalization of the discontinuous slender-body-theory solution introduced by Smith (1977) and others to describe the separated flow over cones and other slender bodies at a slight angle of attack to the oncoming stream. The main difference is that the solution to the present problem would involve distributed vorticity as well as vorticity concentrated in the sheets (see figure 6).

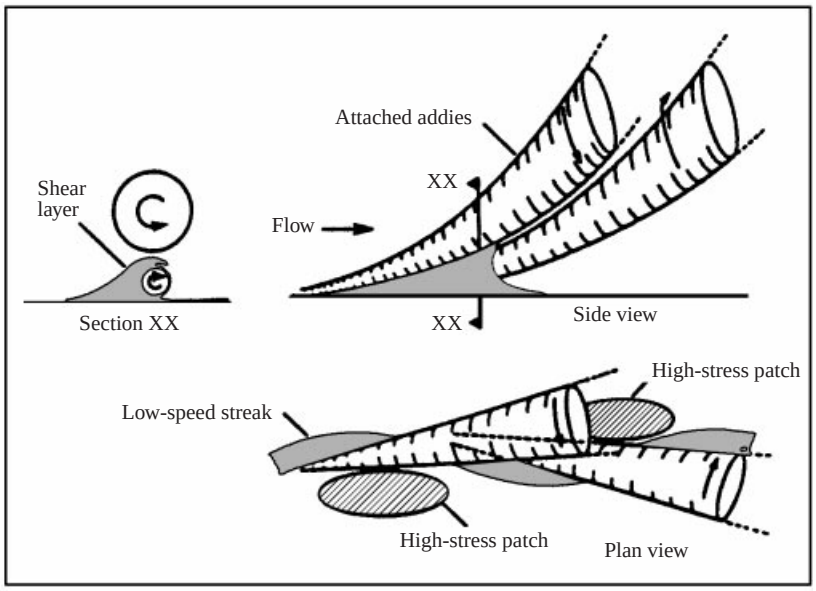

FIGURE 7. Sketch of pattern educed for turbulent channel flow (from Stretch 1991).

Smith (1977) investigated the local vortex-sheet behaviour at the separation line and showed that two types of separation can occur, one of which exhibits a smooth pressure gradient at the surface, and the other of which exhibits an infinite pressure gradient there. The numerical coefficient multiplying the infinite-pressure-gradient term in this solution can be arbitrarily specified. It is determined by extending the analysis to include viscous effects – which are confined to boundary layers at the surface of the body and to thin shear layers along the separated stream surfaces.

Smith (1978) showed that the separation region itself has a triple-deck structure in the cross-flow plane and that the coefficient of the infinite-pressure-gradient term is proportional to $r^{-1/16}$ as $r \to \infty$. Needless to say, this factor will be very close to unity unless r is extremely large, which suggests that the infinite-Reynolds-number limit will not be very robust. However, the boundary-region equations, from which the Smith (1977) and Smith (1978) results can be recovered, are fairly easy to solve numerically, even at large values of r, and it is probably easier to calculate the solutions for large but finite r to these equations than to work out the infinite-r asymptotic solution.

Before leaving this discussion of the large-r limit, it is appropriate to numerically investigate the convergence of the infinite-r asymptotic solution to the finite-r numerical result. We have not worked out the separated stream-surface solution, but since this solution is still parabolic in the streamwise direction, it is the same as the unseparated solution of GL in the region upstream of the separation point. However, the convergence is very slow and becomes worse as the singularity in the solution of GL is approached. It is therefore necessary to include a second term in the asymptotic expansion of GL. This term is worked out in Appendix B.

Figure 8 is a comparison of the spanwise-varying component of the streamwise velocity determined from the full boundary-region equations with the ones determined from the one- and two-term boundary-layer solutions. The calculations are carried out on the $z = 0.91$ plane where the initial singularity in the GL solution occurs and, consequently, where the convergence is expected to be the slowest. The figure shows

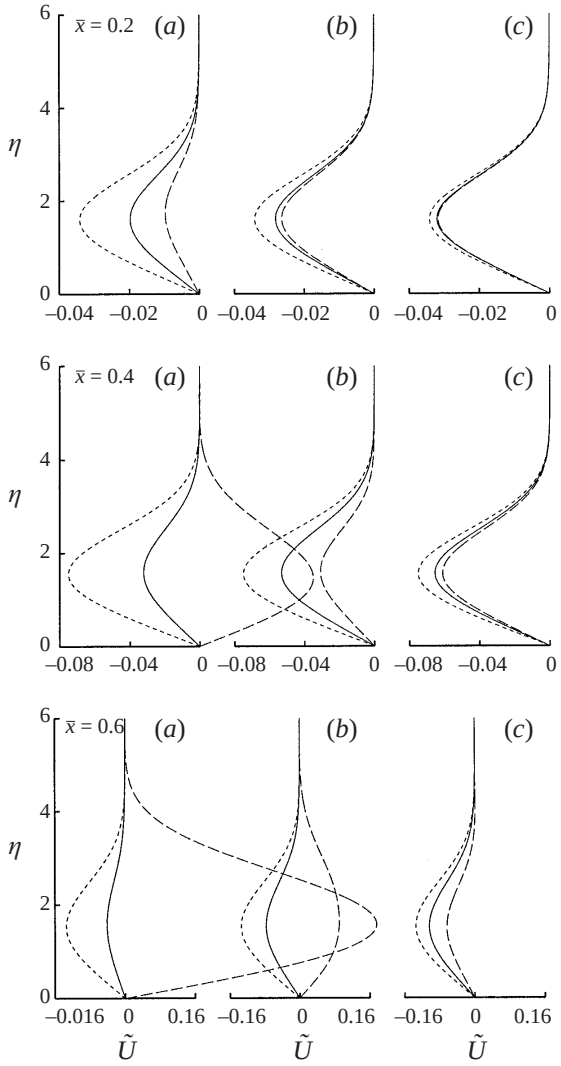

FIGURE 8. Comparison of the spanwise-varying component of the streamwise velocity determined by the boundary-region and boundary-layer solutions along the $z = 0.91$ plane at various $\bar{x}$. Solid lines, boundary-region solution; long-dashed lines, two-term boundary-layer solution; short-dashed lines, one-term boundary-layer solution. (*a*) $r = 10$; (*b*) $r = 100$; (*c*) $r = 1000$.

that even the two-term expansion converges very slowly when $\bar{x} = 0.6$ – indicating that the convergence is non-uniform in $\bar{x}$ as $\bar{x}$ approaches the singularity.

5.2. *Comparison with Klebanoff-mode experiments*

As already indicated, the external flow resulting from the vorticity field (5.1) does not produce a continuous forcing of the boundary-region solution at large streamwise distances and is, therefore, inappropriate to the Klebanoff-mode experiments. It is also not sufficiently complex to represent the random nature of the actual flow. These deficiencies can be corrected by replacing (5.1) with

$$\psi_\infty = \sum_{m=-N}^{+N} \sum_{n=-N}^{+N} \psi_\infty^{(m,n)} e^{i\gamma(mz+ny)}, \tag{5.2}$$

which is periodic, rather than decaying, in the transverse variable y. The true upstream flow can be approximated by taking the Fourier coefficients to be

$$\psi_\infty^{(m,n)} = (1-\delta_{m,0})(1-\delta_{0,n})\,[A(k)]^{1/2}\,\mathrm{e}^{\mathrm{i}\theta_{m,n}}, \tag{5.3}$$

where $\delta_{m,n}$ is the Kronecker delta tensor, $k \equiv \gamma(m^2+n^2)^{1/2}$, $A(k)$ is a spectrum function and $\theta_{m,n}$ is a uniformly distributed random angle. A similar representation was used by Rogallo (1981) to describe an isotropic turbulence field. Here, we express the spectrum function $A(k)$ as

$$A(k) = \frac{C}{4\pi^2}\frac{\mathrm{d}}{k\,\mathrm{d}k}\left\{\frac{\mathrm{d}}{k\,\mathrm{d}k}\left[\frac{\mathrm{e}^{-6.7k/r^{3/4}}}{1+b(2k)^{5/3}}\right]\right\}, \tag{5.4}$$

which is consistent with the Kolmogorov spectrum law at intermediate values of k and agrees with the approximation used by Gulyaev *et al.* (1989) for isotropic turbulence when b is set equal to $1.35/[1+35/(2r)^{3/4}]$. The arbitrary constant C is determined by fixing the value of the kinetic energy

$$E_K \equiv \left(\frac{\gamma}{2\pi}\right)^2 \int_0^{2\pi/\gamma}\int_0^{2\pi/\gamma} \tfrac{1}{2}|\nabla_\perp \psi_\infty|^2 \mathrm{d}y\mathrm{d}z \tag{5.5}$$

of the imposed cross-flow and the transverse scale factor γ is determined by requiring that the non-dimensional characteristic length

$$\left[E_K \Big/ \left(\frac{\gamma}{2\pi}\right)^2 \int_0^{2\pi/\gamma}\int_0^{2\pi/\gamma} \left(\tfrac{1}{2}\nabla_\perp^2 \psi_\infty\right)^2 \mathrm{d}y\mathrm{d}z\right]^{1/2}, \tag{5.6}$$

of that flow be equal to unity. The constants C and γ therefore depend on the disturbance Reynolds number r but not on the random phase angles $\theta_{m,n}$. The mode number N was more or less arbitrarily set equal to 5.

Figure 9 shows the cross-flow streamline pattern corresponding to $r = 50$ (which is appropriate to the well-documented Westin *et al.* 1994 experiment), $E_K = \frac{1}{4}$ and a particular choice of $\theta_{m,n}$. We refer to it as case A. The downstream evolution of this disturbance is determined by numerically solving (3.26) and the analysis of §3 shows that this can be done independently of the boundary-region computation by introducing the transformed cross-stream variable $\hat{y}$. The computation shows that there is a gradual spreading of the initial streamlines as the flow evolves downstream. It also shows that there is a reduction in the higher modes due to viscous dissipation and a gradual shift of the vortex cores due to mutual induction effects.

Figure 10 is a plot of the contours of constant streamwise velocity in the cross-flow plane at the indicated positions for case A. The figure shows that the flow becomes highly distorted in certain very localized regions even at relatively short downstream distances and at a relatively moderate value of the disturbance Reynolds number. This is caused by the broad-band nature of the imposed free-stream disturbance. However, figure 11 shows another set of contours at the same values of r and E_K and the same streamwise locations but with a different choice for the $\theta_{m,n}$. We refer to it as case B. This case, which is more typical than case A, does not exhibit the strong localized distortions found in the latter, which suggests that even small changes in the details of the upstream disturbance can strongly affect the resulting boundary-layer flow.

We have already indicated that our ultimate objective is to explain the behaviour of the flows with high levels of free-stream turbulence, which are, of course, unsteady

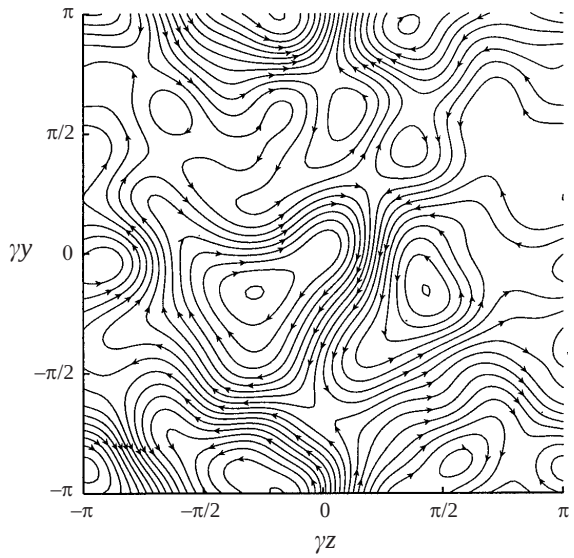

FIGURE 9. Streamline pattern in the cross-flow plane of the imposed steady upstream disturbance field (5.2) for case A.

with stochastically varying upstream boundary conditions. But, as already noted the relevant experiments show that the boundary-layer fluctuations are of very low frequency and it is therefore not unreasonable to expect that the temporal variations in these experiments can be simulated by varying the phases of the upstream boundary conditions in the present study. We show that the results are then consistent with the experimental observations when the flow stability is discussed below.

The strong localized distortions are washed out when the flow is averaged in the spanwise direction to obtain the streamwise velocity fluctuations given by (see (4.1))

$$\tilde{U}_{rms} \equiv \left[\frac{\gamma}{2\pi}\int_0^{2\pi/\gamma} \tilde{U}(\bar{x}, y, z)^2 \mathrm{d}z\right]^{1/2}. \tag{5.7}$$

The resulting flow is then much less sensitive to the details of the upstream distortion as evidenced by figure 12 which shows the peak value of $\tilde{U}_{rms}$ for cases A and B. The curves are much closer than might be expected from the large difference between the contours shown in figures 10 and 11. These differences are reflected in the curves showing the peak local streamwise velocity fluctuation $|\tilde{U}|$ near the z-planes of maximum boundary-layer thickness. The root-mean-square (r.m.s.) and local curves for case A are consistent with the Goldstein & Wundrow (1998) contention that the local streamwise velocity fluctuation can become much larger than the corresponding r.m.s. value.

The r.m.s. velocity fluctuations usually reported in the Klebanoff-mode experiments involve some sort of averaging and might therefore bear some relation to the spanwise-average velocity (5.7) – which could explain why a connection between the Klebanoff modes and the infrequently occurring strong localized distortions has not, as yet, been reported in the literature.

The decrease in wall shear resulting from the movement of low-momentum fluid away from the wall may, ultimately, lead to distinct shear layers in the streamwise velocity profiles. This is shown in figure 13(*a*) which is a plot of the streamwise velocity

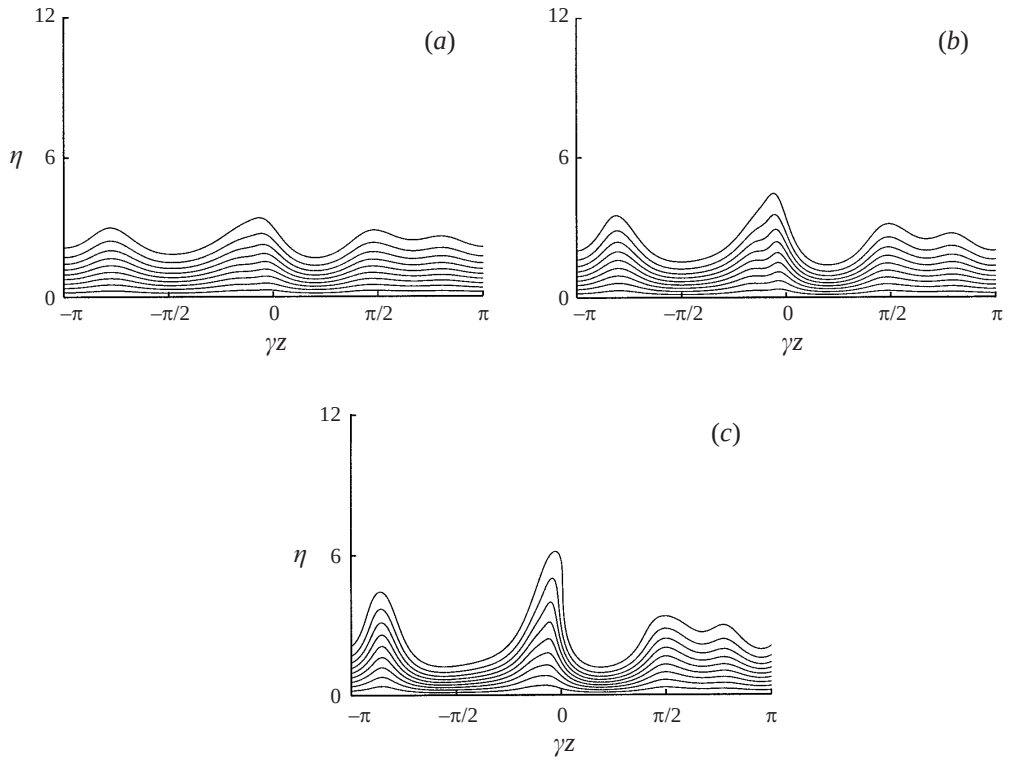

FIGURE 10. Streamwise velocity contours in the cross-flow plane for case A. (*a*) $\bar{x} = 0.6$; (*b*) $\bar{x} = 1.2$; (*c*) $\bar{x} = 2.4$. Nine contours correspond to $U = 0.1, 0.2, \ldots, 0.9$.

profiles near the planes of maximum inflection at $\bar{x} = 2.4$ for cases A and B. Kovasznay *et al.* (1962) showed that the 'high shear layers' observed in their experiment led to the formation of strong negative 'spikes' in the corresponding streamwise velocity traces and ultimately to the formation of turbulent spots. Since the case A profile in figure 13(*a*) closely resembles the distinct shear layers in the instantaneous velocity profiles in figure 9 of Kovasznay *et al.* (1962), we expect it to breakdown in a similar fashion. The profile for case B exhibits no such shear layer and is therefore unlikely to be conducive to turbulent-spot formation. Unfortunately, with the exception of some minimal results in Kendall (1998), the corresponding instantaneous velocity profiles were not reported in most of the more recent Klebanoff-mode experiments (Roach & Brierley 1992; Blair 1992; Westin *et al.* 1994) and we are therefore forced to compare our results with the older Kovasznay *et al.* (1962) data.

Greenspan & Benney (1963) attributed the spike/turbulent-spot formation in the Kovasznay *et al.* (1962) experiment to the growth of inviscid Rayleigh instabilities on the extremely unstable shear layers that were observed in that investigation. They analysed the phenomena by calculating the two-dimensional instability wave growth on an idealized two-dimensional time-dependent base flow that resembled the experimentally observed instantaneous profiles at certain fixed spanwise locations – even though the actual flow was highly three-dimensional. This greatly simplified the computations, as well as the interpretation of the phenomena, but probably made the numerical results very inaccurate. Since our objective here is to explain and not necessarily to accurately predict the experimental observations, we tentatively apply

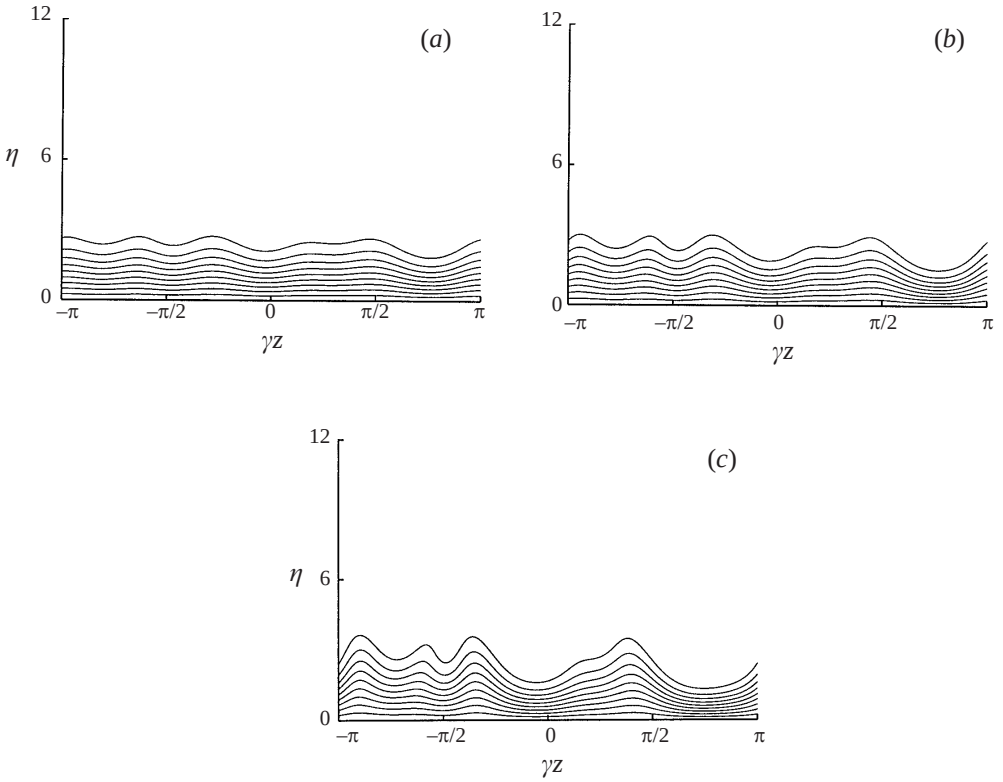

FIGURE 11. Streamwise velocity contours in the cross-flow plane for case B. (*a*) $\bar{x} = 0.6$; (*b*) $\bar{x} = 1.2$; (*c*) $\bar{x} = 2.4$. Nine contours correspond to $U = 0.1, 0.2, \ldots, 0.9$.

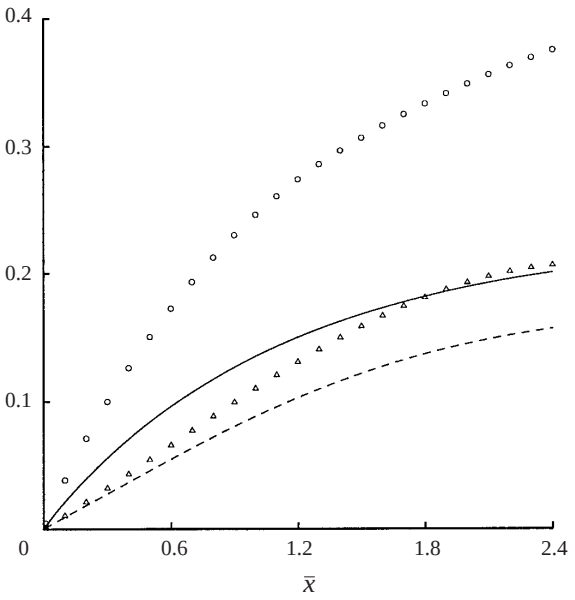

FIGURE 12. Comparison of peak r.m.s. and local streamwise velocity fluctuations for cases A and B. Case A: $\tilde{U}_{rms}$ (solid lines); $|\tilde{U}|$ along $\gamma z = -0.2$ (○). Case B: $\tilde{U}_{rms}$ (dashed lines); $|\tilde{U}|$ along $\gamma z = -1$ (△).

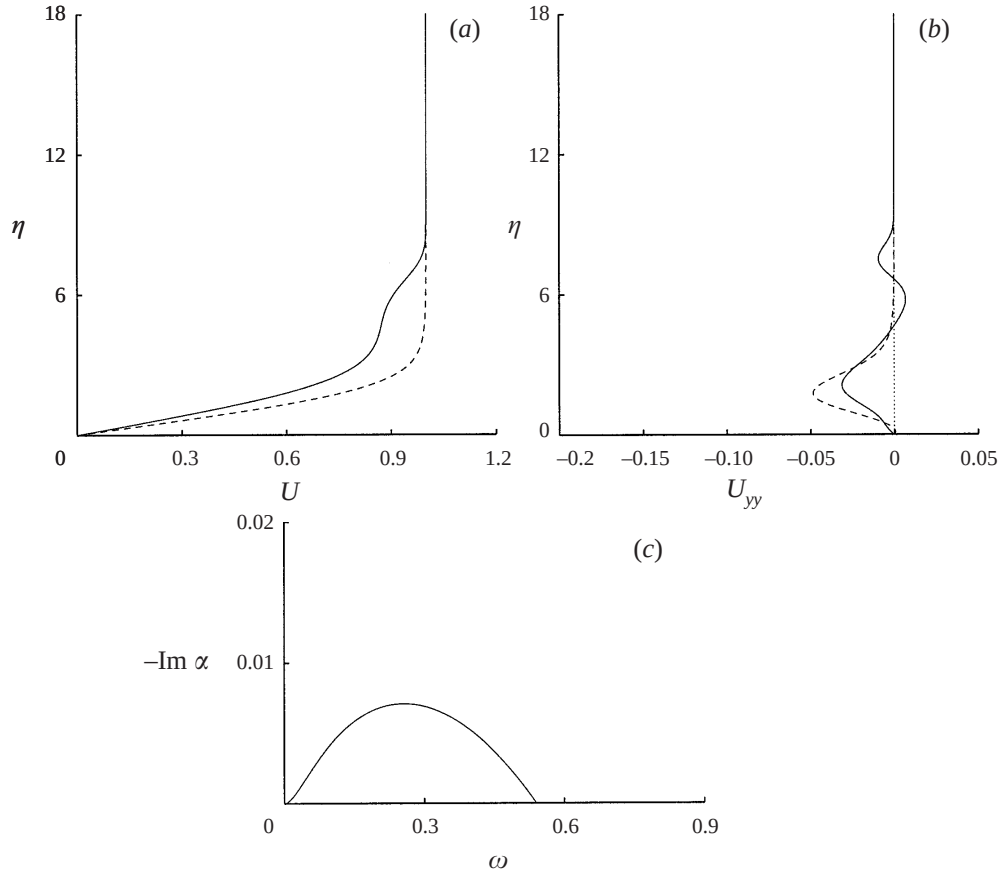

FIGURE 13. Local two-dimensional stability results at $\bar{x} = 2.4$ near planes of maximum inflection for case A (solid lines, $\gamma z = 0$) and case B (dashed lines, $\gamma z = -\pi/2$): (*a*) streamwise velocity profiles; (*b*) second derivatives of streamwise velocity profiles; (*c*) instability wave growth rates.

the locally two-dimensional approximation used by Greenspan & Benney (1963) to the present study.

Since the wavelengths of the resulting two-dimensional instabilities are likely to be of the order of the boundary-layer thickness, they should exhibit growth rates that are, at least, of the order of the reciprocal boundary-layer thickness, which would be much larger than the growth rates of the viscous Tollmien–Schlichting instabilities that would otherwise occur. In fact, even the flattened profiles that occur upstream of the inflectional regions are likely to be more unstable to Tollmien–Schlichting-type instabilities than the undisturbed Blasius profile.

On the other hand, the experimental flows are highly stochastic and should therefore exhibit upstream velocity fluctuations that occasionally become very large relative to the mean. The effects of the higher instantaneous velocities are best accounted for in the present analysis by increasing the kinetic energy of the imposed cross-flow while maintaining a fixed disturbance Reynolds number. This is equivalent to increasing the disturbance Reynolds number and appropriately rescaling the variables. But, since this rescaling is not possible in the actual unsteady problem where the disturbance Reynolds number would be based on the averaged characteristics of the imposed flow, it is probably clearer to interpret the present results as an increased E_K at fixed r. The

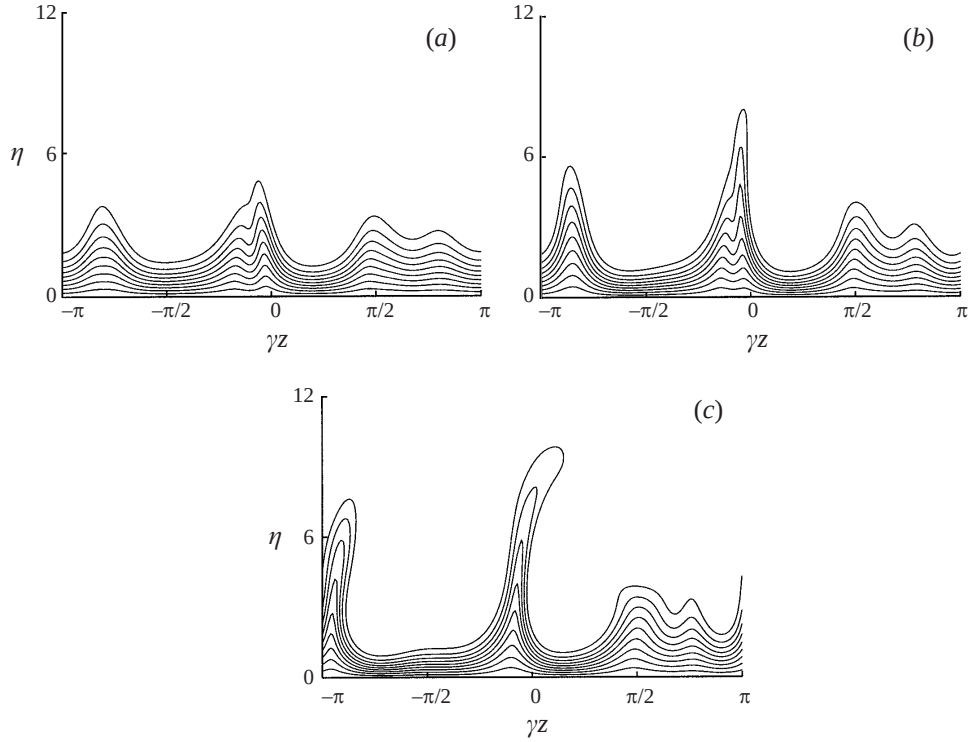

FIGURE 14. Streamwise velocity contours in the cross-flow plane for case C. (*a*) $\bar{x} = 0.6$; (*b*) $\bar{x} = 1.2$; (*c*) $\bar{x} = 2.4$. Nine contours correspond to $U = 0.1, 0.2, \ldots, 0.9$.

contours of constant streamwise velocity corresponding to $E_K = 1$ and the same r and $\theta_{m,n}$ as used in cases A and B are shown in figures 14 and 15. We refer to them as cases C and D, respectively. The four-fold increase in E_K is equivalent to increasing the disturbance Reynolds number to 100 – a value more appropriate to the Blair (1992) experiment discussed below. Figure 16(*a*) shows the corresponding streamwise velocity profiles near the planes of maximum inflection. Notice that the case C profile exhibits a wake-like defect in the upper portion of the boundary layer causing it to be even more unstable than those in figure 13(*a*). The wake defect may correspond to the instantaneous 'backward jets' reported by Jacobs & Durbin (2001). The profile for case D has no such wake defect but it does contain a highly inflectional region near the wall (see figure 16*b*) which is not present in case C.

The case A velocity profile in figure 13(*a*) is inflectional, but the situation for case B is much less obvious. The inflectional nature of the profiles can be seen more clearly from figure 13(*b*), which is a plot of the corresponding second derivatives of U with respect to y. It follows that the case B velocity profile is weakly inflectional near the wall and is therefore expected to be only slightly unstable to the locally two-dimensional inviscid instability waves being considered herein. When interpreting figures 13 and 16, it should be noted that the planes of maximum inflection and maximum boundary-layer thickness are approximately equal for cases A and C but are quite different for cases B and D. The inviscid instability wave growth rates were computed from the plane-wave solutions to the two-dimensional Rayleigh equation

$$\left(\frac{\partial}{\partial t} + U\frac{\partial}{\partial x}\right)\nabla^2\hat{p} - 2U_y\hat{p}_{xy} = 0, \tag{5.8}$$

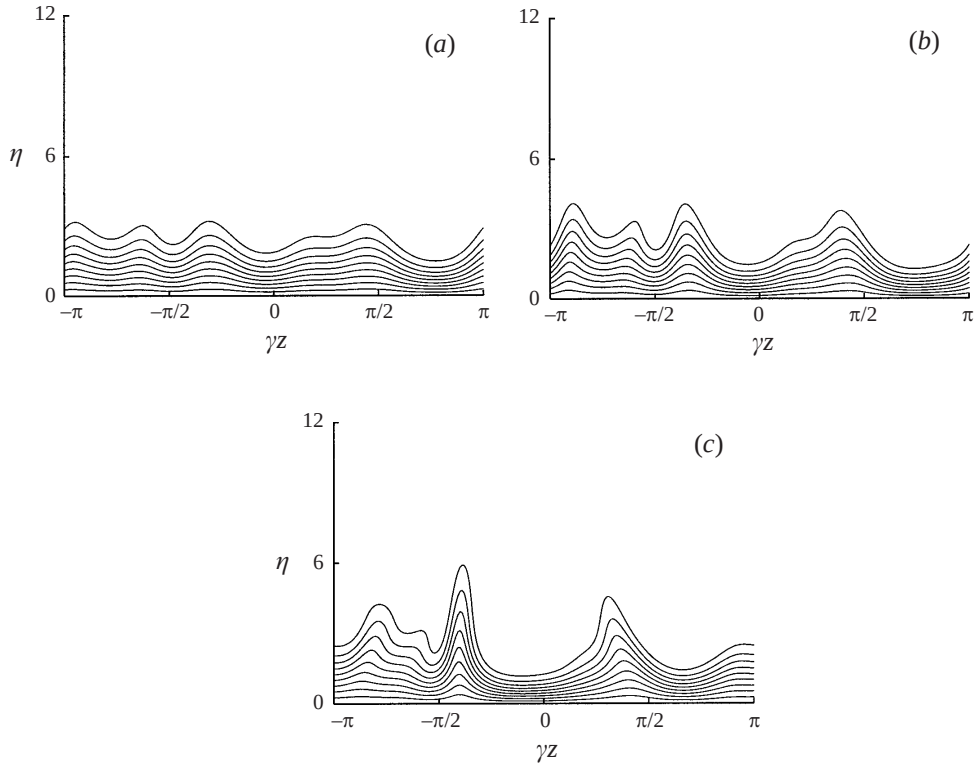

FIGURE 15. Streamwise velocity contours in the cross-flow plane for case D. (*a*) $\bar{x} = 0.6$; (*b*) $\bar{x} = 1.2$; (*c*) $\bar{x} = 2.4$. Nine contours correspond to $U = 0.1, 0.2, \ldots, 0.9$.

scaled by the characteristic boundary-layer thickness $(\sigma\bar{x})^{1/2}$ and are plotted as functions of the scaled Strouhal number in figure 13(*c*) for the case A profile shown in figure 13(*a*). The relatively large value of this spatial growth rate suggests that the instability wave will ultimately develop into a turbulent spot, which would not be the case for the more typical case B profile. This could explain the highly intermittent nature of the spot formation in the Klebanoff-mode type experiments since the instantaneous velocity profiles in these experiments can be identified with the present steady flow profiles calculated at different initial conditions.

This is consistent with the experiments of Westin *et al.* (1994) who report the occasional appearance of turbulent spots at their last measuring station which, for their 1.5% free-stream turbulence level case, corresponds to $\bar{x} \approx 2$ and $r \approx 58$ in the present analysis.

The profiles of figure 16(*a*) are even more unstable than the ones shown in figure 13(*a*). The corresponding spatial growth rates are shown in figure 16(*c*). The instability characteristics of the outer inflectional region in case C are consistent with the experiments carried out by Blair (1992), who imposed a weak favourable pressure gradient on his flow in order to inhibit the growth of Tollmien–Schlichting waves. Blair's most important observation, from our point of view at least, is the appearance of large single and double negative spikes in the time displays of the streamwise velocity in the outer reaches of the boundary layer, which preceded the formation of turbulent spots at the wall. Eventually, the spots did form, but by that time, the outer-region spikes were very intense and well on their way to becoming turbulent.

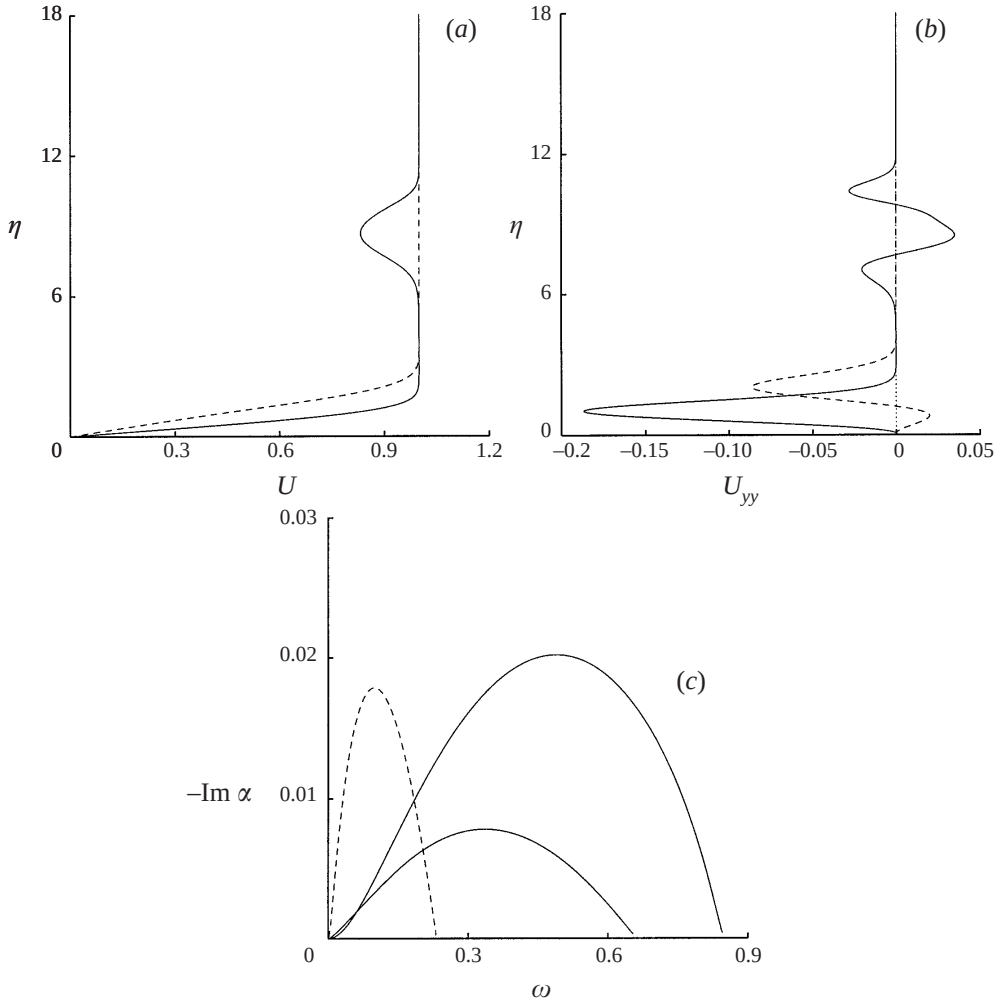

FIGURE 16. Local two-dimensional stability results at $\bar{x} = 2.4$ near planes of maximum inflection for case C (solid lines, $\gamma z = 0.2$) and case D (dashed lines, $\gamma z = \pi/2$). (*a*) streamwise velocity profiles; (*b*) second derivatives of streamwise velocity profiles; (*c*) instability wave growth rates.

Blair attributed these spikes to large-scale coherent structures in the outer reaches of the boundary layer, whose relatively extensive pressure fields could then provoke the incipient turbulent spots or wave packets in the easily destabilized viscous layer at the wall. Our contention here is that these large-scale structures arise, in turn, from the instability of the wake-like profiles just described. Outer-edge disturbances were also reported by Kendall (1998).

Of course, these results are at best only suggestive of the actual phenomena due to the two-dimensional nature of the approximation. The actual stability characteristics would have to be determined by solving a generalized Rayleigh equation (see, for example Hall & Horseman 1991; Balachandar & Malik 1995; Wundrow 1996), whose solutions would probably exhibit somewhat different growth rates than the present results. These solutions are also expected to exhibit spanwise-varying mode shapes that would be maximal in the regions of greatest mean-flow distortion and nearly vanish in the regions where the mean flow approaches its undisturbed state (Hall &

Horseman 1991). The resulting highly concentrated disturbances could then rapidly grow to nonlinear amplitudes and ultimately break down into turbulent spots.

The growth rates of the truly three-dimensional viscous instabilities associated with the spanwise-flow variation (which can be thought of as generalized Tollmien–Schlichting waves when the inflection points are close to the wall) scale with the inverse of the spanwise length scale λ and are therefore likely to be smaller than the Rayleigh growth rates when the disturbance Reynolds number is large. However, the rapidly growing local instabilities could be part of a more global Tollmien–Schlichting wave system that propagates downstream to the inflectional region of the boundary layer from some upstream location where it is initially introduced into the boundary layer, say, as an initially plane wave (Tani & Komoda 1962; Tani & Aihara 1969). The local growth of this wave could still be fairly large in the inflectional region and lead to the formation of turbulent spots even though the average growth of the overall wave could be less than it would be in the absence of the Klebanoff modes. This scenario, which would be most relevant to case D, is consistent with the experimentally observed Tollmien–Schlichting wave growth which appears, on average, to be reduced by the Klebanoff modes (Boiko *et al.* 1994; Kendall 1998). However, when the inflectional region is in the outer part of the boundary layer as in case C, a more likely scenario might be that the instability is initiated locally through some localized receptivity mechanism as suggested by Jacobs & Durbin (2001).

These turbulent-spot-formation mechanisms could be operative in various flow regions up to a free-stream turbulence level of about 5%. Beyond that point, it is impossible to detect any turbulent spots in the boundary layer or, for that matter, any other discernible features of the flow.

The instability of the advected streamwise velocity profiles may also play a role in maintaining the turbulent motion in a fully turbulent boundary layer. A major difference between the Klebanoff modes and the wall-layer streaks in turbulent boundary layers is that the Klebanoff modes are forced by the imposed turbulence in the free stream, whereas the wall-layer streaks are probably self-sustaining due to some kind of feedback mechanism. A possible scenario is that the instability of the ejected flow breaks down into an external turbulent flow which then drives the wall-layer streaks in the same way that free-stream turbulence drives the Klebanoff modes.

The present work is the culmination of a decade long study of the Klebanoff-mode phenomena by the authors and their colleagues. Many researchers have contributed to this effort in some fashion. But worthy of acknowledgement are Professors Eli Reshotko and Paul Durbin for their encouragement and helpful comments and Dr James Kendall for pointing out the connection of the original GL analysis to the Klebanoff-mode phenomena at the 1992 Transition Study Group meeting in Reno, encouraging the authors to pursue this connection and finally supplying the smoke-flow visualization photograph along with other useful information. It is also appropriate to acknowledge Dr Stephen Cowley for providing a critical review of the manuscript, pointing out some crucial references that the authors overlooked, and most importantly for insisting that they contrast the present study with related work that has appeared during the course of this activity and thereby significantly improve the quality of the manuscript.

Appendix A. Upstream-matching conditions

In this appendix, the upstream-matching conditions for the boundary-region problem (3.3)–(3.6) are derived. Using (2.3)–(2.5) and (2.20)–(2.22) and putting $\varphi = \psi_0 + \pi_0$

shows that matching with the linear solutions of §2 requires

$$U \to 1, \tag{A 1}$$

$$V \to \sigma\beta\Delta^{-1} + \psi_{0z}(y,z) - \beta\Delta\varphi_{yz}(y,z), \tag{A 2}$$

$$W \to -\psi_{0y}(y,z) + \beta\Delta\varphi_{yy}(y,z), \tag{A 3}$$

$$P \to \tfrac{1}{4}\sigma\beta\bar{x}^{-1}(2\eta-\beta) + \sigma\beta\Delta^{-1}\pi_{0z}(y,z), \tag{A 4}$$

as $\bar{x} \to 0$, with y held fixed at $O(1)$, and (2.12)–(2.14) show that

$$U \to F' - \psi_{0yz}(0,z)\tfrac{1}{2}\bar{x}\eta F'' + \bar{x}\Delta U_1(\eta,z), \tag{A 5}$$

$$V \to \sigma\Delta^{-1}(\eta F' - F) - \psi_{0yz}(0,z)\tfrac{1}{4}\Delta G + \sigma\bar{x}V_1(\eta,z), \tag{A 6}$$

$$W \to -\psi_{0y}(0,z)F' + \Delta W_1(\eta,z), \tag{A 7}$$

as $\bar{x} \to 0$ with $\eta = y/\Delta$ held fixed at $O(1)$, where the higher-order terms $\{U_1, V_1, W_1\}$, which are derived below from the boundary-region equations themselves, have been included because they are needed to successfully start the numerical solution discussed in §4.

To obtain the matching condition for P as $\bar{x} \to 0$ with η held fixed, it is first noted that the upstream boundary-layer pressure fluctuations consist of two independent components. The first results from the interaction of the imposed vorticity field with the displaced flow above the boundary layer, and the second arises from a higher-order correction to the Blasius flow. Crow (1966) gives an analytic expression for the latter component, and it is easy to show from conservation of momentum that the former component must be independent of η. Combining these results leads to

$$P \to \sigma^2\Delta^{-2}\left(\eta F'' + \eta F F' - F^2 + \tfrac{1}{2}\beta^2\right) + \sigma\beta\Delta^{-1}\pi_{0z}(0,z), \tag{A 8}$$

as $\bar{x} \to 0$, with η held fixed at $O(1)$.

Equations (A 1)–(A 4) and (A 5)–(A 8) can be combined to form a composite solution to the boundary-region problem that is uniformly valid in y as $\bar{x} \to 0$. However, it is first necessary to determine the higher-order terms $\{U_1, V_1, W_1\}$. Rewriting the boundary-region equations (3.3)–(3.6) in terms of the independent variables $\bar{x}$, η and z, substituting (A 5)–(A 8) into the result, and equating like powers of $\bar{x}$ shows that $\{U_1, V_1, W_1\}$ are governed by

$$3U_1 - \eta U_{1\eta} + V_{1\eta} + 2W_{1z} = 0, \tag{A 9}$$

$$\left(3F' - \eta F''\right)U_1 - F U_{1\eta} + F'' V_1 = U_{1\eta\eta}, \tag{A 10}$$

$$F' W_1 - F W_{1\eta} + \beta\pi_{0zz}(0,z) = W_{1\eta\eta}, \tag{A 11}$$

which must be solved subject to the no-slip condition

$$U_1 = V_1 = W_1 = 0 \quad \text{at} \quad \eta = 0, \tag{A 12}$$

and, in order to match onto the small-y expansions of (A 1)–(A 3), the solutions must satisfy

$$U_1 \to 0, \quad W_1 \to -\psi_{0yy}(0,z)(\eta-\beta) \quad \text{as} \quad \eta \to \infty. \tag{A 13}$$

Equations (A 9)–(A 13) describe a linear boundary-value problem in η which must be solved numerically in general.

A set of composite expansions that is uniformly valid in y as $\bar{x} \to 0$ can now be constructed by adding the outer solutions (A 1)–(A 4) to the inner solutions (A 5)–(A 8)

and subtracting off the terms they have in common (Van Dyke 1975). The common parts are determined, in the usual way, by comparing the small-y expansions of (A 1)–(A 4) with the large-η expansions of (A 5)–(A 8). The spanwise-varying components of the resulting composite expansions are given by (4.8)–(4.11) where

$$U_c \equiv U_1, \tag{A 14}$$

$$W_c \equiv W_1 + \psi_{0yy}(0,z)(\eta - \beta), \tag{A 15}$$

and, in arriving at (4.9), use was made of the fact that $\pi_{0y}(0,z) = -\frac{3}{4}\psi_{0y}(0,z)$ which follows from the definitions (2.23) and (2.24).

Appendix B. The high-disturbance Reynolds-number limit

This appendix is concerned with the high-disturbance Reynolds-number limit of the boundary-region problem (i.e. the limit as $\sigma \to 0$). In this limit, the flow in region III develops a double-layer structure consisting of an inviscid upper layer in which y is $O(1)$ and a viscous lower layer in which y is $O(\sigma^{1/2})$.

The form of the upper-layer velocity field can be deduced from the small-σ behaviour of (A 1)–(A 3) and is given by

$$\{U, V, W\} = \{1, \breve{v}_0, \breve{w}_0\}(\bar{x}, y, z) + \sigma^{1/2}\{0, \breve{v}_1, \breve{w}_1\}(\bar{x}, y, z) + \cdots. \tag{B 1}$$

The corresponding pressure field expands like

$$P = \breve{p}_0(\bar{x}, y, z) + \sigma^{1/2}\breve{p}_1(\bar{x}, y, z) + \cdots. \tag{B 2}$$

Substituting (B 1) and (B 2) into the boundary-region equations (3.3)–(3.6) and equating like powers of σ shows that the upper-layer cross-flow must satisfy

$$\breve{v}_{0y} + \breve{w}_{0z} = 0, \tag{B 3}$$

$$\breve{v}_{0\bar{x}} + \breve{v}_0\breve{v}_{0y} + \breve{w}_0\breve{v}_{0z} + \breve{p}_{0y} = 0, \tag{B 4}$$

$$\breve{w}_{0\bar{x}} + \breve{v}_0\breve{w}_{0y} + \breve{w}_0\breve{w}_{0z} + \breve{p}_{0z} = 0, \tag{B 5}$$

at leading order, and

$$\breve{v}_{1y} + \breve{w}_{1z} = 0, \tag{B 6}$$

$$\breve{v}_{1\bar{x}} + \breve{v}_0\breve{v}_{1y} + \breve{w}_0\breve{v}_{1z} + \breve{v}_{0y}\breve{v}_1 + \breve{v}_{0z}\breve{w}_1 + \breve{p}_{1y} = 0, \tag{B 7}$$

$$\breve{w}_{1\bar{x}} + \breve{v}_0\breve{w}_{1y} + \breve{w}_0\breve{w}_{1z} + \breve{w}_{0y}\breve{v}_1 + \breve{w}_{0z}\breve{w}_1 + \breve{p}_{1z} = 0, \tag{B 8}$$

at $O(\sigma^{1/2})$. Equations (A 2) and (A 3) imply that the solutions to these equations must satisfy

$$\breve{v}_0 = \psi_{0z}(y,z), \quad \breve{w}_0 = -\psi_{0y}(y,z) \quad \text{at} \quad \bar{x} = 0, \tag{B 9}$$

and, putting $\bar{\Delta} = (2\bar{x})^{1/2}$,

$$\breve{v}_1 \to \beta\bar{\Delta}^{-1} - \beta\bar{\Delta}\varphi_{yz}(y,z), \quad \breve{w}_1 \to \beta\bar{\Delta}\varphi_{yy}(y,z) \quad \text{as} \quad \bar{x} \to 0, \tag{B 10}$$

in order to reduce to the linear rapid-distortion solution upstream. Equations (B 3)–(B 5) are just the two-dimensional, time-dependent Euler equations with $\bar{x}$ playing the role of the time and are equivalent to (3.6)–(3.8) of GL.

The appropriately scaled transverse variable in the lower layer is

$$Y \equiv y/\sigma^{1/2} = O(1), \tag{B 11}$$

which is related to the Blasius variable η by $\eta = Y/\bar{\Delta}$. The small-σ behaviour of (A 5)–(A 7) implies that the velocity field in the lower layer is of the form

$$\{U, V, W\} = \{\check{U}_0, \sigma^{1/2}\check{V}_0, \check{W}_0\}(\bar{x}, Y, z) + \sigma^{1/2}\{\check{U}_1, \sigma^{1/2}\check{V}_1, \check{W}_1\}(\bar{x}, Y, z) + \cdots, \quad \text{(B 12)}$$

and (B 2) implies that the corresponding pressure field should expand like

$$P = \check{P}_0(\bar{x}, Y, z) + \sigma^{1/2}\check{P}_1(\bar{x}, Y, z) + \cdots. \quad \text{(B 13)}$$

Substituting (B 11)–(B 13) into the boundary-region equations and equating like powers of σ shows that

$$\check{U}_{0\bar{x}} + \check{V}_{0Y} + \check{W}_{0z} = 0, \quad \text{(B 14)}$$

$$\check{U}_0\check{U}_{0\bar{x}} + \check{V}_0\check{U}_{0Y} + \check{W}_0\check{U}_{0z} = \check{U}_{0YY}, \quad \text{(B 15)}$$

$$\check{U}_0\check{W}_{0\bar{x}} + \check{V}_0\check{W}_{0Y} + \check{W}_0\check{W}_{0z} + \check{P}_{0z} = \check{U}_{0YY}, \quad \text{(B 16)}$$

at leading order, and

$$\check{U}_{1\bar{x}} + \check{V}_{1Y} + \check{W}_{1z} = 0, \quad \text{(B 17)}$$

$$\check{U}_0\check{U}_{1\bar{x}} + \check{V}_0\check{U}_{1Y} + \check{W}_0\check{U}_{1z} + \check{U}_{0\bar{x}}\check{U}_1 + \check{U}_{0Y}\check{V}_1 + \check{U}_{0z}\check{W}_1 = \check{U}_{1YY}, \quad \text{(B 18)}$$

$$\check{U}_0\check{W}_{1\bar{x}} + \check{V}_0\check{W}_{1Y} + \check{W}_0\check{W}_{1z} + \check{W}_{0\bar{x}}\check{U}_1 + \check{W}_{0Y}\check{V}_1 + \check{W}_{0z}\check{W}_1 = \check{W}_{1YY}, \quad \text{(B 19)}$$

at $O(\sigma^{1/2})$. The first two orders of the normal-momentum equation show that $\check{P}_0$ and $\check{P}_1$ must be independent of Y.

Equations (B 14)–(B 16) are just the three-dimensional, boundary-layer equations used in GL. It is worth noting that (B 12) and (B 13) contain an $O(\sigma^{1/2})$ correction induced by boundary-layer displacement effects which for fixed ϵ can be interpreted as $O(R_\lambda^{-1/2})$. This is in contrast to two-dimensional, boundary-layer flows where the first correction does not come in until $O(R_\lambda^{-1})$ and shows that the boundary-layer approximation is less robust in three dimensions than in two.

Matching with (A 5)–(A 7) implies that

$$\check{U}_0 \to F' - \psi_{0yz}(0, z)\tfrac{1}{2}\bar{x}\eta F'', \quad \text{(B 20)}$$

$$\check{V}_0 \to \bar{\Delta}^{-1}(\eta F' - F) - \psi_{0yz}(0, z)\tfrac{1}{4}\bar{\Delta}G, \quad \text{(B 21)}$$

$$\check{W}_0 \to -\psi_{0y}(0, z)F', \quad \text{(B 22)}$$

and

$$\check{U}_1 \to \bar{x}\bar{\Delta}U_1(\eta, z), \quad \check{V}_1 \to \bar{x}V_1(\eta, z), \quad \check{W}_1 \to \bar{\Delta}W_1(\eta, z), \quad \text{(B 23)}$$

as $\bar{x} \to 0$. The solutions to (B 14)–(B 19) must also satisfy the no-slip condition

$$\check{U}_0 = \check{V}_0 = \check{W}_0 = 0, \quad \check{U}_1 = \check{V}_1 = \check{W}_1 = 0 \quad \text{at} \quad Y = 0, \quad \text{(B 24)}$$

and they must match onto the small-y behaviour of (B 1) which requires that

$$\check{U}_0 \to 1, \quad \check{W}_0 \to \check{w}_0(\bar{x}, 0, x), \quad \check{U}_1 \to 0, \quad \check{W}_1 \to \check{w}_{0y}(\bar{x}, 0, z)Y + \check{w}_1(\bar{x}, 0, z), \quad \text{(B 25)}$$

as $Y \to \infty$, and since $\check{P}_0$ and $\check{P}_1$ are independent of Y

$$\check{P}_0 = \check{p}_0(\bar{x}, 0, z), \quad \check{P}_1 = \check{p}_1(\bar{x}, 0, z), \quad \text{(B 26)}$$

where use has been made of the fact that $\check{p}_{0y}(\bar{x}, 0, z) = 0$ which follows from (B 4) and (B 27) below.

Using (B 14) and (B 25) to derive the large-Y behaviour of $\check{V}_0$ shows that matching

the second components of (B 1) and (B 12) requires that the upper-layer solution must satisfy the boundary condition

$$\check{v}_0 = 0, \quad \check{v}_1 = -\int_0^\infty \left[\check{U}_{0\bar{x}} + \check{W}_{0z} - \check{w}_{0z}(\bar{x}, 0, z)\right] \mathrm{d}Y \quad \text{at} \quad y = 0, \tag{B 27}$$

which implies that

$$\check{v}_0, \check{w}_0, \check{v}_1, \check{w}_1 \to 0, \quad \text{as} \quad y \to \infty, \tag{B 28}$$

for the imposed vorticity field (5.1) that is of interest here.

The upper-layer Euler problems are solved using the scheme described in GL, and the reader is referred to that reference for the details. The corresponding boundary-layer problems are solved using an algorithm based on the one described in §4.

REFERENCES

Andersson, P., Berggren, M. & Henningson, D. S. 1999 Optimal disturbances and bypass transition in boundary layers. *Phys. Fluids* **11**, 134–150.

Balachandar, S. & Malik, M. R. 1995 Inviscid instability of streamwise corner flow. *J. Fluid Mech.* **282**, 181–201.

Benney, D. J. 1984 The evolution of disturbances in shear flows at high Reynolds numbers. *Stud. App. Maths* **70**, 1–19.

Bertolotti, F. P. 1997 Response of the Blasius boundary layer to free-stream vorticity. *Phys. Fluids* **9**, 2286–2299.

Blair, M. F. 1992 Boundary-layer transition in acceleration flows with intense freestream turbulence: Part 1 – Disturbances upstream of the transition onset. *Trans. ASME*: *J. Fluids Engng* **114**, 313–321.

Boiko, A. V., Westin, K. J. A., Klingmann, B. G. B., Kozlov, V. V. & Alfredsson, P. H. 1994 Experiments in a boundary layer subjected to free stream turbulence. Part 2. The role of TS-waves in the transition process. *J. Fluid Mech.* **281**, 219–245.

Cantwell, B. J., Coles, D. E. & Dimotakis, P. E. 1978 Structure and entrainment in the plane of symmetry of a turbulent spot. *J. Fluid Mech.* **87**, 641–672.

Cebeci, T., Khattab, A. K. & Stewartson, K. 1981 Three-dimensional laminar boundary layers and the ok of accessibility. *J. Fluid Mech.* **107**, 57–87.

Choudhari, M. M. 1996 Boundary-layer receptivity to three-dimensional unsteady vortical disturbances in free stream. *AIAA Paper* 96-0181.

Crow, S. C. 1966 The spanwise perturbation of two-dimensional boundary-layers. *J. Fluid Mech.* **24**, 153–164.

Dryden, H. L. 1936 Air flow in the boundary layer near a plate. *NACA Rep.* 562.

Goldstein, M. E. 1978 Unsteady vortical and entropic distortions of potential flows round arbitrary obstacles. *J. Fluid Mech.* **89**, 433–468.

Goldstein, M. E. 1997 Response of the pretransitional laminar boundary layer to free-stream turbulence. Otto Laporte lecture. *Bull. Am. Phys. Soc.* **42**(11), 2150.

Goldstein, M. E. & Choi, S. W. 1989 Nonlinear evolution of interacting oblique waves on two-dimensional shear layers. *J. Fluid Mech.* **207**, 97–120. Also Corrigendum *J. Fluid Mech.* **216**, 659–663.

Goldstein, M. E. & Leib, S. J. 1993 Three-dimensional boundary-layer instability and separation induced by small-amplitude streamwise vorticity in the upstream flow. *J. Fluid Mech.* **246**, 21–41 (referred to herein as GL).

Goldstein, M. E., Leib, S. J. & Cowley, S. J. 1992 Distortion of a flat-plate boundary layer by free-stream vorticity normal to the plate. *J. Fluid Mech.* **237**, 231–260.

Goldstein, M. E. & Wundrow, D. W. 1998 On the environmental realizability of algebraically growing disturbances and their relation to Klebanoff modes. *Theor. Comput. Fluid Dyn.* **10**, 171–186.

Greenspan, H. P. & Benney, D. J. 1963 On shear-layer instability, breakdown and transition. *J. Fluid Mech.* **15**, 133–153.

Gulyaev, A. N., Kozlov, V. E., Kuznetson, V. R., Mineev, B. I. & Sekundov, A. N. 1989 Interaction of a laminar boundary layer with external turbulence. *Izv. Akad. Nauk SSSR Mekh. Zhid. Gaza* **6**, 700–710.

Hall, P. & Horseman, N. J. 1991 The linear inviscid secondary instability of longitudinal vortex structures in boundary layers. *J. Fluid Mech.* **232**, 357–375.

Hall, P. & Smith, F. T. 1991 On strongly nonlinear vortex/wave interactions in boundary-layer transition. *J. Fluid Mech.* **227**, 641–666.

Jacobs, R. G. & Durbin, P. A. 2001 Simulations of bypass transition. *J. Fluid Mech.* (in press).

Kemp, N. H. 1951 The laminar three-dimensional boundary layer and a study of the flow past a side edge. MAeS Thesis, Cornell University.

Kendall, J. M. 1985 Experimental study of disturbances produced in a pre-transitional laminar boundary layer by weak free stream turbulence. *AIAA Paper* 85-1695.

Kendall, J. M. 1991 Studies on laminar boundary layer receptivity to freestream turbulence near a leading edge. In *Boundary layer Stability and Transition to Turbulence* (ed. D. C. Reda, H. L. Reed & R. Kobayashi). ASME FED, vol. 143, pp. 23–30.

Kendall, J. M. 1998 Experiments on boundary-layer receptivity to freestream turbulence. *AIAA Paper* 98-0530.

Kerschen, E. J. & Balsa, T. F. 1981 Transformation of the equation governing disturbances of a two-dimensional compressible flow. *AIAA J.* **19**(10), 1367–1370.

Kline, S. J., Reynolds, W. C., Schraub, F. A. & Runstadler, P. W. 1967 The structure of turbulent boundary layers. *J. Fluid Mech.* **30**, 741–773.

Kovasznay, L. S. G., Komoda, H. & Vasudeva, B. R. 1962 Detailed flow field in transition. In *Proceedings of the 1962 Heat Transfer and Fluid Mechanics Institute* (ed. F. E. Ehlers, J. J. Kauzlarich, C. A. Sleicher, Jr. & R. E. Street), pp. 1–26. Stanford University Press.

Landahl, M. T. 1977 Dynamics of boundary layer turbulence and the mechanism of drag reduction. *Phys. Fluids* **20**, 55–63.

Leib, S. J., Wundrow, D. W. & Goldstein, M. E. 1999 Effects of free-stream turbulence and other vortical disturbances on a laminar boundary layer. *J. Fluid Mech.* **380**, 169–203.

Luchini, P. 1996 Reynolds-number-independent instability of the boundary layer over a flat surface. *J. Fluid Mech.* **327**, 101–115.

Luchini, P. 2000 Reynolds-number-independent instability of the boundary layer over a flat surface: optimal perturbations. *J. Fluid Mech.* **404**, 289–309.

Mankbadi, R. R., Wu, X. & Lee, S. S. 1993 A critical-layer analysis of the resonant triad in boundary-layer transition: nonlinear interactions *J. Fluid Mech.* **256**, 85–106.

Noble, B. 1958 *Methods Based on the Wiener–Hopf Technique for the Solution of Partial Differential Equations.* Pergamon.

Roach, P. E. & Brierley, D. H. 1992 The influence of a turbulent free stream on zero pressure gradient transitional boundary layer development. Part I: Test cases T3A and T3B. In *Numerical Simulation of Unsteady Flows and Transition to Turbulence* (ed. O. Pironneau, W. Rodi, I. L. Ryhming, A. M. Saville & T. V. Truong), pp. 319–347. Cambridge University Press.

Rogallo, R. S. 1981 Numerical experiments in homogeneous turbulence. *NASA Tech. Memo.* 81315.

Smith, C. R. & Abbott, D. E. (Eds.) 1979 *Coherent Structures of Turbulent Boundary Layers.* Lehigh University.

Smith, F. T. 1978 Three-dimensional viscous and inviscid separation of a vortex sheet from a smooth non-slender body. *RAE Tech. Rep.* 78095.

Smith, J. H. B. 1977 Behaviour of a vortex sheet separating from a smooth surface. *RAE Tech. Rep.* 77058.

Stretch, D. 1991 Automated pattern eduction from turbulent flow diagnostics. *Ann. Res. Briefs–* 1990. Center for Turbulence Research, Stanford University.

Tani, I. & Aihara, Y. 1969 Görtler vortices and boundary-layer transition. *Z. Angew. Math. Phys.* **20**, 609–618.

Tani, I. & Komoda, H. 1962 Boundary-layer transition in the presence of streamwise vortices. *J. Aerospace Sci.* **29**, 440–444.

Taylor, G. I. 1939 Some recent developments in the study of turbulence. In *Proceedings of the Fifth International Congress for Applied Mechanics* (ed. J. P. Den Hartog & H. Peters), pp. 294–310. Wiley.

Van Dyke, M. D. 1975 *Perturbation Methods in Fluid Mechanics.* Parabolic.

Westin, K. J. A., Boiko, A. V., Klingmann, B. G. B., Kozlov, V. V. & Alfredsson, P. H. 1994 Experiments in a boundary layer subjected to free stream turbulence. Part 1. Boundary layer structure and receptivity. *J. Fluid Mech.* **281**, 193–218.

Wu, X. 1993 On critical-layer and diffusion-layer nonlinearity in the three-dimensional stage of boundary-layer transition. *Proc. R. Soc. Lond.* A **443**, 95–106.

Wu, X., Jacobs, R. G., Hunt, J. C. R. & Durbin, P. A. 1999 Simulation of boundary layer transition induced by periodically passing wakes. *J. Fluid Mech.* **398**, 109–153.

Wundrow, D. W. 1996 Linear instability of a uni-directional transversely sheared mean flow. *NASA CR* 198535.